博士論文

論文題目

Study on extracellular vesicles-mediated regulation of the physical barriers.

(細胞外小胞による生体バリアの制御に関する研究)

氏名

富永　直臣

Study on extracellular vesicles-mediated regulation of the physical barriers

(細胞外小胞による生体バリアの制御に関する研究)

Supervisor:

Professor Hitoshi Nakagama 中釜　斉　教授

Graduate school of Medicine, 医学系研究科

The University of Tokyo 東京大学

April, 2014 entrance 平成２４年４月入学

Doctor of Medical Science course 医学博士課程

Department of Pathology 病因・病理学専攻

Naoomi Tominaga 富永直臣

Table of Contents

1. List of Abbreviations

BBB : blood-brain barrier

BRB : Blood-Retinal Barrier

BTB : Blood-Testis Barrier

cDNA : complementary DNA

CIP : Calf Intestinal Alkaline Phosphatase

cRNA : complementary RNA

Cy3 : cyanine 3

D3H1 : MDA-MB-231-luc-D3H1

D3H2LN : MDA-MB-231-luc-D3H2LN

EVs : extracellular vesicles

FBS : fetal bovine serum

HE : hematoxylin and eosin

HUVECs : human umbilical vascular endothelial cells

i.p.: intraperitoneal

i.v.: intravenously

IVIS : *in vivo* imaging system

miR, miRNA : microRNA

NaF : sodium fluorescein

nSMase2 : neutral sphingomyelinase 2

Papp : apparent permeability coefficient

PDGF-B : platelet-derived growth factor B

PFA : paraformaldehyde

RNAi : RNA interference

TEER : transendothelial electrical resistance

TEM : Transmission electron microscope

TGF-β : transforming growth factor-β

TJs : tight junctions

VEGF : Vascular endothelial growth factor

2. Abstract

A key event during brain metastasis is the migration of cancer cells through blood-brain barrier (BBB), which consists of the endothelium and surrounding cells. The transfer of cancer cell-derived extracellular vesicles (EVs) represents a novel mechanism of communication between cancer cells and normal cells. However, the contribution of EVs to brain metastasis is still unclear. Here, I show that EVs promote brain metastasis by causing the destruction of BBB. Using an *in vitro* BBB model, I demonstrated that the knockdown of genes responsible for EV production inhibited invasion into the parenchymal side of BBB, thus suggesting that EVs contribute to cancer invasion into the parenchymal region. EVs from established brain metastatic cell lines (BMD), compared with EVs from the original cell line, increased the permeability of BBB, as assessed by transendothelial electrical resistance (TEER) and the permeability of a fluorescent dye. I demonstrated that systemic injection of BMD cell-derived EVs promoted brain metastasis of breast cancer cell lines *in vivo*. I also found that miR-181c in EVs promoted the destruction of tight junction and adherens junction proteins. Interestingly, miR-181c promoted the destruction of BBB through the abnormal localization of actin via the down-regulation of its target gene *PDPK1*. PDPK1 degradation by miR-181c leads to down-regulation of phosphorylated cofilin and the resultant activation of cofilin-induced

modulation of actin dynamics. Together, these results indicate a novel mechanism of brain metastasis that triggers the destruction of BBB mediated by EVs.

3. Background

Extracellular vesicles

Extracellular vesicles (EV)s mediate cell-cell communication via the delivery of their contents, which include proteins, mRNAs, and microRNAs (miRNAs)[1] (Fig. A). In the past two decades, EVs (including exosomes) have emerged as novel mediators of cell-cell communication in cancer biology. EVs were first reported in 1983 by Johnstone and colleagues, who made this discovery while culturing reticulocytes[2]. Despite these novel findings, it took more than a decade[3] for appreciation of their general significance to extend beyond the reticulocyte/transferrin receptor model[4]. EVs are nanometer-sized (50–100 nm) membranous vesicles that are known to regulate multiple aspects of malignancy in cancer cells[5-7]. Peinado *et al.* have reported that cancer-derived EVs educate bone marrow cells, resulting in the promotion of metastasis of melanoma cells to the lung[7]. Melanoma-derived EVs also induce vascular leakiness at pre-metastatic sites and reprogramm bone marrow progenitors toward a pro-vasculogenic phenotype that is positive for c-Kit, the receptor tyrosine kinase Tie2 and Met. miRNA-containing EVs have recently become noteworthy for their involvement in EV-mediated cell-cell communication[1,8-10]. Although the contribution of EVs to cancer metastasis is evident, little is known regarding the roles of EVs in brain metastasis.

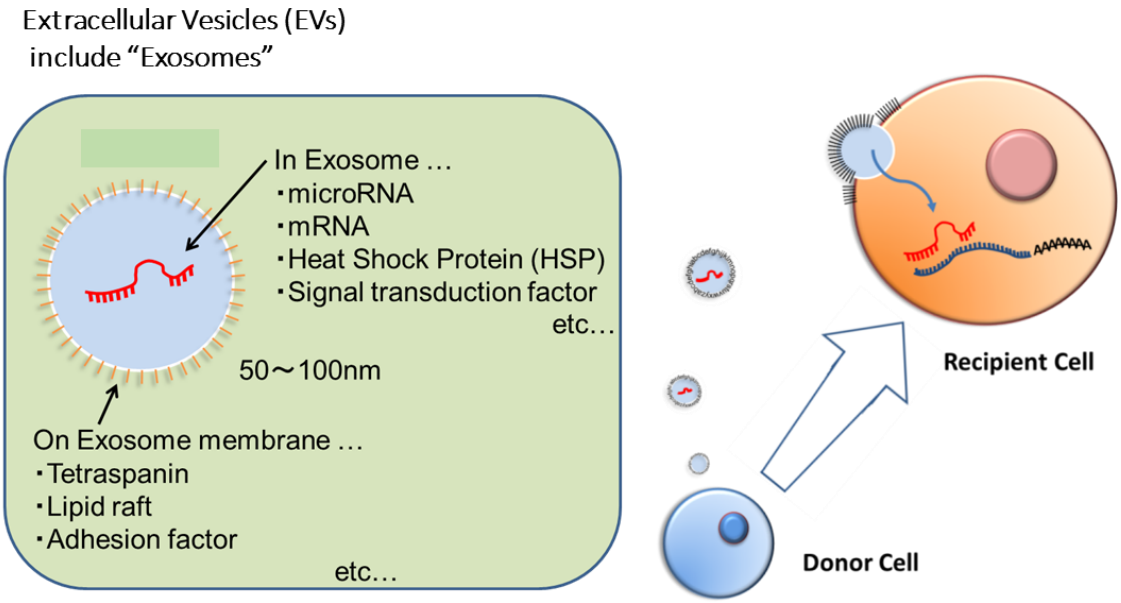

Fig A. Schematic model of extracellular vesicles

EVs are microvesicles of approximately 100 nm that are secreted from cells. EVs contain several types of functional molecules, including proteins, mRNAs and miRNAs. Secreted EVs are incorporated into recipient cells, where they deliver the functional molecules. This figure was modified from The Igaku No Ayumi (vol.249, no.5, p388; 2014/5/3).

microRNA

miRNAs are non-coding RNAs of 20-25 nucleic acids in length, which are translated from genomic DNA and mature through several processing steps (Fig. B). Mature miRNA inhibits the translation of its target mRNA after forming a complex with Dicer, which is an RNase III enzyme. This mechanism is known as RNA interference (RNAi)[11,12]. miRNA-containing EVs mediate many biological functions[10,13,14]. Kosaka *et al.* have reported that miR-210, which is contained within breast cancer cell-derived EVs, can be transferred to human umbilical vascular endothelial cells (HUVECs) and can induce HUVEC capillary formation. Furthermore, miR-210-containing EVs also promote angiogenesis *in vivo* and metastasis to the lungs[8]. EVs from cancer cells affect these steps through the modulation of host immune system, angiogenesis and pre/pro-metastatic niche formation[1,8,13].

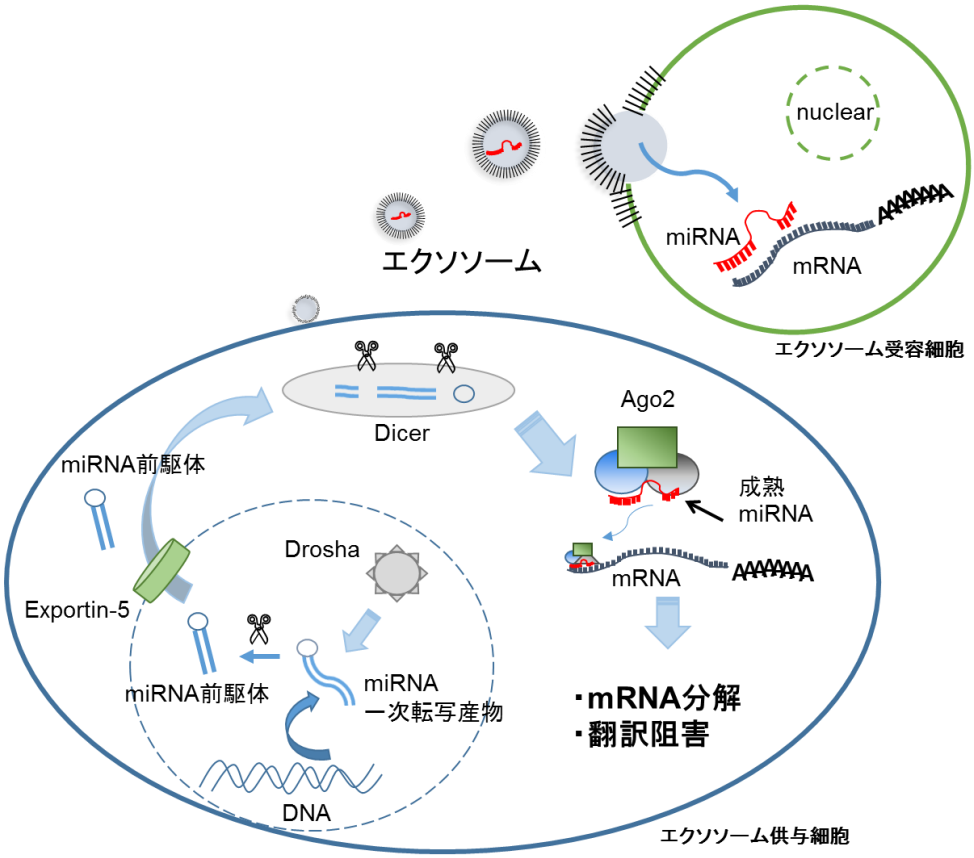

Fig B. Schematic model of RNA interference

RNA interference is one mechanism of gene regulation. EVs that contain miRNA affect protein expression in recipient cells.

This figure was modified from The Igaku No Ayumi (vol.249, no.5, p388; 2014/5/3).

Physical barrier

Blood-brain barrier (BBB) is a physical barrier (Fig. C). The total length of blood vessels in the brain is estimated to be approximately 600-700 km in adult humans[13]. Brain blood vessel is formed by brain endothelial cells, brain pericytes, and astrocytes. BBB has three features in common with other blood vessels: "(1) tight junctions (TJs) of extremely low permeability; (2) low rates of fluid-phase endocytosis; and (3) specific transport and carrier molecules"[15]. The basic structure of the BBB is maintained by the TJs of brain endothelial cells. These TJs are composed of specific molecules, such as Claudin-5, Occludin, and ZO-1[16]. This structure strictly limits the movement of molecules from the blood to the brain parenchyma side[17]. Furthermore, the brain endothelial cells themselves have features such as specific transporters and low rates of endocytosis that restricts the movement of these molecules. The establishment of BBB requires signaling from pericytes[16,18] and astrocytes[16]. For example, the cross-talk between brain endothelial cells and pericytes by platelet-derived growth factor B (PDGF-B), transforming growth factor-β (TGF-β), Notch, sphingosine-1 phosphate and angiopoietin signaling is essential for the formation of the BBB. Furthermore, structures similar to the BBB exist in the body and include Blood-Retinal Barrier (BRB)[19], and Blood-Testis Barrier (BTB)[20].

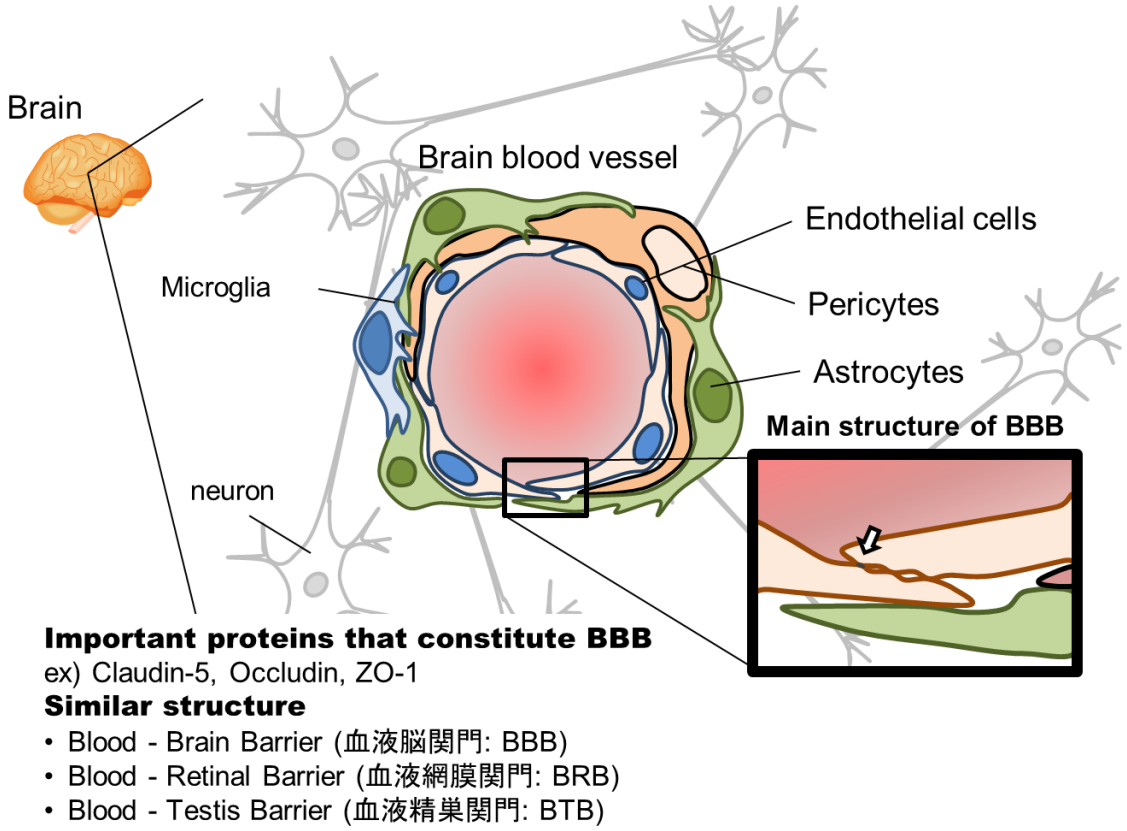

Fig C. Schematic model of blood-brain barrier

Brain blood vessels consist of endothelial cells, pericytes and astrocytes. The main structure of blood-brain barrier is maintained by tight junctions between endothelial cells. However, pericytes and astrocytes are also important for the formation of BBB. Structures similar to BBB exist in the retina and testis.

This figure was modified from The Vascular Biology & Medicine (vol.16, no.2, p25; 2015/6).

Brain metastasis of breast cancer

The rate of clinically apparent brain metastasis in breast cancer patients has been reported to be 14-30%[21]. The apparent incidence of brain metastases has also been reported to be increasing[21]. Furthermore, brain metastasis is associated with a particularly poor prognosis of cancer patients. Nevertheless, the mechanisms of brain metastasis are not clearly understood. Therefore, novel insights into the brain metastatic process are needed. A key event during brain metastasis is the migration of cancer cells through BBB[22,23], which consists of the endothelium and surrounding cells[24,25] (Fig. C). BBB limits the passive diffusion of molecules. One of the key features of brain metastasis is the destruction of BBB[26]. Tumor cells recognize and bind to components of the vascular membrane, thereby initiating their extravasation; subsequently, the cancer cells invade through the BBB, and new growth at secondary organ sites begins[27,28]. This process suggests that the intact endothelium can serve as a defensive barrier against the extravasation of tumor cells. Although these hypotheses are accepted, the exact molecular mechanisms that trigger brain metastasis are poorly understood. Humoral factors including vascular endothelial growth factor (VEGF) were proposed to mediate the interaction between cancer cells and BBB-constructed cells, resulting in the destruction of BBB structure. The action of VEGF does not fully explain the destruction of BBB

during brain metastasis considering form the complexity of the interactions among cells that compose BBB[29]. Since, it is not known how EVs are annotated with brain metastasis, I hypothesized that cancer-derived EVs regulate brain metastasis of cancer cells.

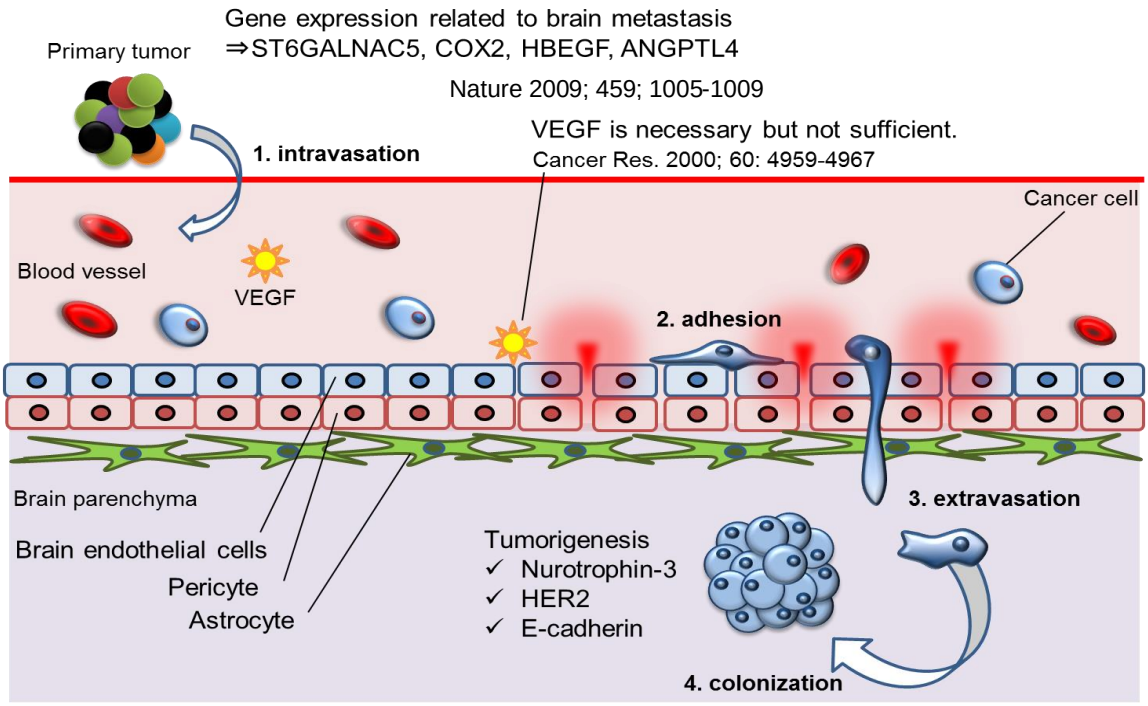

Fig D. Schematic model of brain metastasis

A widely supported hypothesis is that tumor cells recognize and bind to components within the vascular membrane, after which they initiate invasion and the beginning of new growth at secondary organ sites. However, it is difficult for tumor cells to invade the brain parenchyma, because brain vessels have a natural barrier. Though humoral factors, such as vascular endothelial growth factor (VEGF), are important factors for BBB breakdown and brain metastasis, they are not sufficient.

This figure was modified from The Experimental Medicine (vol.33, no.16, p2622; 2015/10).

4. Materials and Methods

Isolation of brain metastatic cells

A cell suspension containing 2×10^5 MDA-MB-231-luc-D3H2LN breast cancer cells in a volume of 100 μl was injected into the left cardiac ventricle of anesthetized 7-week-old C.B-17 Icr-scid/scid female mice. Tumor development was monitored by weekly bioluminescence imaging using the IVIS Spectrum (Caliper Life Science, Hopkinton, MA). Brain metastatic lesions were confirmed by histological analysis after necropsy. Brain lesions were localized by *ex vivo* bioluminescence imaging and resected under sterile conditions. Half of the tissue was fixed with 4% paraformaldehyde (PFA) and processed for histological analysis. The other half was minced and placed in RPMI1640 culture medium (Gibco) containing antibiotic-antimycotic agents and 10% fetal bovine serum (FBS). The cells were briefly centrifuged, resuspended in 0.025% trypsin-EDTA (Gibco), and incubated for an additional 10 min at 37 °C. The cells were resuspended in a culture medium containing 50 μg ml^{-1} Zeocin (Gibco) and were allowed to grow to confluence on a 10-cm dish. BMD2a and BMD2b cells were sorted for further propagation in culture or inoculation in mice. All animal work followed a protocol approved by the NCC Institutional Animal Care and Use Committee (T12-005, T12-005-M01).

Cell culture

MDA-MB-231-luc-D3H1 (purchased from Xenogen Co., CA), MDA-MB-231-luc-D3H2LN (purchased from Xenogen Co., CA), BMD2a, and BMD2b (established from MDA-MB-231-luc-D3H2LN) breast cancer cell lines were cultured in RPMI1640 medium and supplemented with 10% heat-inactivated FBS (Invitrogen) and antibiotic-antimycotic agents at 37 °C in 5% CO_2. These cell lines express luciferase and Zeocin resistance genes.

Transwell invasion assay

For invasion assays, 2×10^4 cells were plated in the top chamber with a Matrigel-coated membrane (24-well insert, BD Biosciences, NJ, USA). Cancer cells were plated in RPMI1640 medium without FBS, and RPMI1640 medium supplemented with 10% FBS (for all other cells) was used as a chemoattractant in the lower chamber. The cells were incubated for 24 hrs, and cells that did not migrate or invade through the pores were removed using a cotton swab. Cells on the lower surface of the membrane were stained with the Diff-Quick Staining Set (Sysmex, Hyogo, Japan) and counted. All assays were performed in triplicate. The data are expressed as the invasion percentage through the

Matrigel matrix and membrane relative to migration through the control membrane, according to the manufacturer's instructions.

Preparation of conditioned medium and EVs

Prior to the collection of cultured medium, MDA-MB-231-luc-D3H1, MDA-MB-231-luc-D3H2LN, BMD2a, and BMD2b cells were washed three times with Advanced RPMI containing antibiotic-antimycotic agents and 2 mM L-glutamine (medium A), and the medium was switched to fresh medium A. After incubation for 2 days, the medium was collected and centrifuged at 2000 ×g for 10 min at 4 ℃. To thoroughly remove cellular debris, the supernatant was filtered with a 0.22-μm Stericup (Millipore, MA, USA). To prepare the EVs, the conditioned medium was ultracentrifuged at 110,000 ×g for 70 min at 4 ℃. The pellets were washed with 11 ml of phosphate-buffered saline and resuspended in phosphate-buffered saline (PBS) after ultracentrifugation. The fraction containing the EVs was measured for its protein content using the Micro BCA protein assay kit (Thermo Scientific, MA, USA).

Count of particle number and size distribution

The number and size distribution of particles were measured using NanoSight particle

tracking system (LM10-HSBF, NanoSight Ltd., UK). Purified EVs by ultracentrifugation were diluted 100~500 times with PBS (-). The diluted EVs liquid sample was injected into NanoShight system. Then Brownian motion of EVs was detected using blue lazar and the CCD camera attached to microscopy. The calculation of particle number and size was performed by NTA 2.3 Analytical Software.

Transmission Electron Microscope

The analysis of EVs by Transmission electron microscope (TEM) was carried out by Terabase Inc. Purified EVs by ultracentrifugation were re-suspended in PBS. Then, re-suspended EVs samples were used for TEM analysis. EVs samples were embedded in ice on grid using Vitrobot (EFI inc., USA). Then these samples were observed with TEM (JEOL-JEM-2200FS).

PKH67-labeled EV transfer

Purified EVs derived from MDA-MB-231-luc-D3H2LN, BMD2a, and BMD2b cells were labeled with a PKH67 green fluorescent labeling kit (Sigma Aldrich, MO, USA). EVs were incubated with 2 μM of PKH67 for 5 min, washed five times using a 100 kDa filter (Microcon YM-100, Millipore) to remove excess dye, and incubated for 24 hrs in

the *in vitro* BBB model at 37 °C in 5% CO_2.

In vitro blood–brain barrier model

To investigate the function of EVs, the BBB kit (MBT24-H) was used as an *in vitro* blood–brain barrier model (PharmaCo-Cell Co. Ltd., Nagasaki, Japan, http://www.pharmacocell.co.jp/). The transendothelial electrical resistance (TEER) value exceeded 150 Ω・cm^2, which indicates that this system could be used as an *in vitro* BBB model.

Transendothelial electrical resistance study

The BBB function of the *in vitro* BBB model was quantified by its TEER. The resistance values (Ω) were measured with an ohmmeter (Millicell ERS-2, Millipore). The TEER values were calculated by means of the unit area resistance:

$R = (A - B) \times 0.33\ cm^2$

$R = TEER(\Omega \cdot cm^2)$

A = measurement resistance value (Ω)

B = blank resistance value (Ω)

Permeability assay

I used a method modified from a previously described permeability assay[31]. After the addition of 200 μl of NaF (10 μg ml^{-1}, Sigma Aldrich) to the upper chamber, as well as the addition of 900 μl of DPBS-H (Dulbecco's PBS (Mg^{+}, Ca^{+}) and 10 mM HEPES, 4.5 mg ml^{-1} D-glucose) to the lower chamber, the plate was incubated with shaking at 37 °C. After 30 min, the DPBS-H of the lower chamber was dispensed into a black plate (n = 8). These samples were measured with a multi-detection monochrometer microplate reader (485 / 535 nm, SAFIRE, Tecan), and the apparent permeability coefficient (Papp) was calculated as follows:

$Papp = (VA \cdot [C]A) \cdot A^{-1} \cdot [C]Luminal^{-1} \cdot t^{-1}$

VA: volume of abluminal chamber (0.9 cm^3)

A: membrane surface area (0.33 cm^2)

[C]Luminal: initial luminal tracer concentration (μg ml^{-1})

[C]A: abluminal tracer concentration (μg ml^{-1})

t: time of experiment (min)

***In vivo* permeability assay**

Purified EVs derived from MDA-MB-231-luc-D3H2LN and BMD2a cells were labeled

with a XenoLight DiR (#125964, Summit Pharmaceuticals International Co.). EVs were incubated with 10 mM of XenoLight DiR for 15 min and washed five times using a 100 kDa filter (Microcon YM-100, Millipore) to remove excess dye. A XenoLight DiR-labeled EV, 5 μg in a volume of 100 μl, was injected into the tail vein of anesthetized 7-weeks-old C.B-17 Icr-scid scid mice. After 6 hrs, 100 μl of Tracer-653 probe (TR-1001, Molecular Targeting Technologies Inc., PA, USA) was injected into the tail vein of mice. After 24 hrs, mice were refluxed to remove excess dye in the blood and were monitored by fluorescence imaging using the IVIS Spectrum (Caliper Life Science, Hopkinton, MA).

Transwell invasion assay using the *in vitro* BBB model

Breast cancer cell invasion was assessed in an *in vitro* BBB model (PharmaCo-Cell Co. Ltd., Nagasaki, Japan). Cancer cells were trypsinized for the invasion assay and labeled with PKH26 (Sigma Aldrich) when using the *in vitro* BBB model. Cancer cells (2×10^4 cells) were plated in Ham's F-12 (Gibco) medium without serum, and medium supplied by the *in vitro* BBB model kit containing 10% serum was used as the chemoattractant in the lower chamber. After 48 hrs, non-invading cells were removed with cotton swabs, and the nuclei were stained with Hoechst 33342 (Dojindo, Kumamoto, Japan). The PKH26 fluorescence of invading cells was subsequently counted. All assays were performed in

triplicate.

siRNA transfection

RAB27B, neutral sphingomyelinase 2 (nSMase2), and both siRNA transfections of BMD2a cells were performed using the DharmaFECT transfection reagent (Thermo Scientific) according to the manufacturer's protocol. A total of 25 nM of siRNA was used for each transfection. After 24 hrs, the transfected cells were used for each assay. miR-181c (Ambion, ID: MC10181; AACAUUCAACCUGUCGGUGAGU) and *PDPK1* (Ambion, ID: S10275; UUUCUCACAGCCUAACCGCT) siRNA were transfected into the cells using DharmaFECT transfection reagent. The cells were treated with the siRNA at the concentration of 25 nM.

RNA isolation and detection of miRNA and mRNA

Total RNA containing abundant small RNAs was isolated from the cultured cells and the sera of patients using RNeasy Mini Kit (Qiagen). EVs from patients' sera were isolated with Total Exosome Isolation (from serum) (Invitrogen). The expression of mRNA and miRNA was assessed by qRT-PCR as described previously[14]. PCR was carried out in 96-well plates using Real-Time PCR System 7300 (Applied Biosystems, CA, USA). All

reactions were performed in triplicate. All TaqMan MicroRNA assays were purchased from Applied Biosystems. RNU6 was used as an internal control. The expression levels of miR-181c and RNU6 were measured by qRT-PCR using a Universal PCR Master Mix (Applied Biosystems). Gene expression was analyzed using TaqMan Gene Expression Assays (Applied Biosystems). The expression of *RAB27B*, *nSMase2*, *β-actin*, *PDPK1*, and *GAPDH* was measured by qRT-PCR using a Platinum Quantitative PCR SuperMix (Applied Biosystems). Primers and probes were defined as follows: *RAB27B* (Assay ID: Hs01072206_m1), *nSMase2* (Assay ID: Hs00920354_m1), *actin-beta* (Assay ID: Hs01060665_g1), *PDPK1* (Assay ID: Hs00176884_m1), and *GAPDH* (Assay ID: Hs02758991_g1). *GAPDH* was used as an internal control.

Western blot

Proteins were isolated from cells using M-PER (Thermo Scientific, MA, USA) separated in Mini-PROTEAN TGX Gel (4–12%, Bio-Rad) and electrotransferred onto a PVDF membrane (Millipore) at 100v, 1hr. After blocking in Blocking One (Nacalai Tesque, Kyoto, Japan), the membranes were incubated for 1 hr at room temperature with primary antibodies, which included anti-CD63 (purified mouse anti-human CD63, H5C6, 1:200, BD), anti-CD9 (ALB6, 1:200, Santa Cruz Biotechnology Inc.), anti-cytochrome C

(purified mouse anti-cytochrome C, 7H8.2C12, 1:200, BD), anti-Claudin-5 (Z43.JK, 1:200, Invitrogen), anti-Occludin (ZMD.481, 1:200, Invitrogen), anti-ZO-1 (H-300, 1:100, Santa Cruz Biotechnology), anti-N-cadherin (3B9, 1:500, Invitrogen), anti-PDPK1 (#3062, 1:500, Cell Signaling), anti-GAPDH (6C5, 1:1000, Millipore), anti-Cofilin (D3F9, 1:1000, Cell Signaling), anti-Phospho-Cofilin (Ser3) (#3311, 1:500, Cell Signaling), and anti-N-SMase2 (H-195, 1:200, Santa Cruz Biotechnology Inc.). Secondary antibodies (HRP-linked anti-mouse IgG, NA931 or HRP-linked anti-rabbit IgG, NA934, GE Healthcare) were used at a dilution of 1:2000. The membrane was then exposed to ImmunoStar LD (Wako, Osaka, Japan). The chemiluminescence was detected with LAS-2000 (Fujifilm, Japan)

Immunofluorescence staining

Endothelial cells from the *in vitro* BBB model were fixed with 3% PFA in PBS for 10 min at room temperature and treated with PBS containing 0.1% Triton-X100 for 10 min after being washed with PBS containing Mg^{2+} and Ca^{2+} to permeabilize the cells. After fixation, the cells were incubated with 3% BSA in PBS for 1 hr to block the nonspecific binding of antibodies. Subsequently, the endothelial cells were incubated with rabbit polyclonal antibodies against Claudin-5 (Z43.JK, Invitrogen, CA, USA), Occludin

(ZMD.467, Invitrogen), ZO-1 (ZMD.437, Invitrogen), and N-cadherin (3B9, Invitrogen) at 37 °C for 1 hr. After washing with PBS containing Mg^{2+} and Ca^{2+}, they were incubated with Alexa Fluor 594-conjugated anti-rabbit IgG (Invitrogen) for 1 hr at 37 °C. Actin was stained with ActinGreen 488 ReadyProbes Reagent (R37110, Molecular Probes). The stained cells were then washed in PBS without Mg^{2+} and Ca^{2+} and were mounted in VECTASHIELD Mounting Medium (H-1200, Vector Laboratories, CA, USA) for observation under a confocal microscope (FluoView FV1000, Olympus, Tokyo, Japan).

PDPK1 3'UTR luciferase reporter assay

The 3'UTR of *PDPK1* was amplified from total RNA extracted from brain endothelial cells of the *in vitro* BBB model. PCR primers used to amplify the 3'UTR include Forward: AACTCGAGAATGCTGGCTATTGTTGGCCTC and Reverse: AAGCGGCCGCAAGATTAAATCACTGACCCAATAG. The PCR products were cloned into a pGEM-T Easy Vector (Promega, WI, USA). The amplified 3'UTR was cloned downstream of the Renilla luciferase coding region in the psiCHECK-2 (Promega). Human umbilical vein endothelial cells (HUVEC) cells were seeded in 96-well plates 24 hrs prior to transfection. The following day, 100 ng of reporter plasmids along with 100 nM of pre-miR-181c was co-transfected using DharmaFECT Duo transfection reagent

(Thermo Scientific). HEK293 cells were cultured at a density of 5×10^4 cells per well in 96-well tissue culture plates overnight. Cells were collected 24 hrs after transfection and assayed for luciferase activity using EnVision (PerkinElmer, MA, USA). To assess precursor miRNA's effect on reporter activity, 100 ng of synthetic precursor miRNA (pre-miR) (Ambion, Invitrogen) was co-transfected. All experiments were performed in triplicate.

Microarrays

miRNA expression of EVs

Total RNA was extracted from EVs using QIAzol reagent and miRNeasy Mini Kit (Qiagen). The quantity and quality of RNA were determined using NanoDrop ND-1000 spectrophotometer (Thermo Fisher Scientific Inc.) and Agilent Bioanalyzer (Agilent Technologies) according to the recommendations of the manufacture. Total RNA was labeled with cyanine 3 (Cy3) using miRNA Complete Labeling and Hyb Kit (Agilent Technologies) following the manufacturer's instructions. Briefly, 100 ng of total RNA was dephosphorylated using Calf Intestinal Alkaline Phosphatase (CIP) Master Mix, and incubated at 37 ℃ for 30 min. Dephosphorylated RNA was denatured by the incubation with DMSO at 100 ℃ for 5 min, and then immediately transfers to on ice for 2 min. These

products were mixed with a Ligation master mix together with T4 RNA Ligase and Cy3-pCp (Cyanine 3-Cytidine biphosphate), and incubated at 16 ℃ for 2 hours. Labeled RNA was dried using vacuum concentrator at 55 ℃ for 1.5 hours. Cy3-pCp-labeled RNA was hybridized on Agilent SurePrint G3 Human miRNA 8x60K Rel.19 (design ID: 046064). After washing, microarray slides were scanned using an Agilent DNA microarray scanner. Intensity values of each scanned feature were quantified using Agilent Feature Extraction software version 10.7.3.1, which performs background subtractions. I used features that were flagged as no errors (Detected flags) and excluded features that were negative (Not Detected flags). This expression analysis was performed with Agilent GeneSpring GX version 12.6.1. There are a total of 2,006 miRNA probes on SurePrint G3 Human miRNA 8x60K Rel.19 (design ID: 046064) without control probes. I applied ≥2-fold change in signal intensity to identify the significant differences of gene expression in this study. Raw and normalized microarray data are available in the Gene Expression Omnibus (GEO) database (accession numbers GSE63445).

mRNA expression of cells

Total RNA was extracted from cultured brain endothelial cells before EVs or miR-181c treatment using the QIAzol reagent and the miRNeasy Mini Kit (Qiagen). RNA quantity

and quality were determined using a NanoDrop ND-1000 spectrophotometer (Thermo Fisher Scientific Inc.) and an Agilent Bioanalyzer (Agilent Technologies), as recommended. Total RNA was amplified and labeled with cyanine 3 (Cy3) using Low Input Quick Amp Labeling Kit, one-color (Agilent Technologies) following the manufacturer's instructions. Briefly, 100 ng of total RNA was reversed-transcribed to double-strand complementary DNA (cDNA) using a poly dT-T7 promoter primer. Primer, template RNA, and quality-control transcripts of known concentration and quality were first denatured at 65 ℃ for 10 min and incubated for 2 hours at 40 ℃ with 5× first strand buffer, 0.1 M dithiothreitol, 10 mM deoxynucleotide triphosphate mix, and AffinityScript RNase Block Mix. The AffinityScript enzyme was inactivated at 70 ℃ for 15 min. cDNA products were then used as templates for *in vitro* transcription to generate fluorescent complementary RNA (cRNA). cDNA products were mixed with a transcription master mix in the presence of T7 RNA polymerase and Cy3-labeled CTP (cytidine 5′-triphosphate) and incubated at 40 ° C for 2 hours. Labeled cRNA was purified using RNeasy Mini Spin Columns (Qiagen) and eluted in 30 μl of nuclease-free water. After amplification and labeling, cRNA quantity and cyanine incorporation were determined using a NanoDrop ND-1000 spectrophotometer and an Agilent Bioanalyzer. For each hybridization, 0.60 μg of Cy3-labeled cRNA was fragmented and hybridized at 65 ℃ for

17 hours to an Agilent Cynomolgus macaque Gene Expression Profiling Array (design ID: 028520). After washing, microarray slides were scanned using an Agilent DNA microarray scanner. Intensity values of each scanned feature were quantified using Agilent Feature Extraction software version 10.7.3.1. I used features that were flagged as no errors (Detected flags) and excluded features that were not positive, not significant, not uniform, not above background, saturated, and population outliers (Compromised and Not Detected flags). Normalization was performed with Agilent GeneSpring GX version 12.6.1 (per chip: normalization to 75th percentile shift; per gene: normalization to median of all samples). There are a total of 12,243 probes on Agilent Cynomolgus macaque Gene Expression Profiling Array (design ID: 028520) without control probes. The altered transcripts were quantified using the comparative method. I applied ≥2-fold change in signal intensity to identify the significant differences of gene expression in this study. Raw and normalized microarray data are available in the Gene Expression Omnibus (GEO) database (accession numbers GSE63447).

Patient serum samples

Collection and usage of human serum from breast cancer patients (n = 56) by the National Cancer Center Institute of Japan were approved by the Institutional Review Board

(No.2013-111). Serum was aliquoted and stored at -80℃ until used, and freeze-thawing was avoided as much as possible after that. Informed consent was obtained from all patients.

5. Results

Establishment of brain metastasis breast cancer cell lines

To identify the influence of EVs on BBB during breast cancer metastasis, we employed MDA-MB-231-luc-D3H2LN cells (D3H2LN), which are human mammary tumor cells with a high tumorigenic and metastatic capacity[8,30] to produce a new brain high-metastatic cell line. D3H2LN cells were injected into immunodeficient female mice by intracardiac (*i.c.*) injections to isolate populations of cells that colonized in the brain (Fig. 1a).

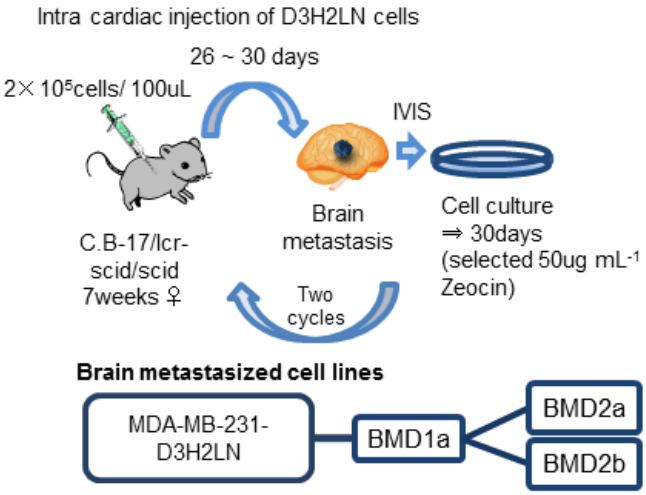

Fig 1a.

Schematic representation of the protocol for the *in vivo*-selected brain metastatic derivatives. MDA-MB-231-D3H2LN breast cancer cell lines (2×10^5 cells) were injected intracardially into C.B-17 Icr-scid scid mice. After 26–30 days, the brain metastasis of cancer cells was monitored by *in vivo* imaging system (IVIS). The brain-metastasized cancer cells were recovered and cultured for approximately 30 days in culture medium containing 50 μg ml-1 Zeocin. This selection was performed twice, and I named the established cell lines BMD2a and BMD2b.

Brain metastasis was monitored by *in vivo* imaging using intraperitoneal (*i.p.*) luciferin injections (Fig. 1b). Cancer cell colonization of the brain tissue was also confirmed by hematoxylin and eosin (HE) staining (Fig. 1c). After tumor dissociation and expansion in culture, the resulting cell populations (brain metastatic derivative 1a, BMD1a) were subjected to a second round of *in vivo* selection, yielding brain metastatic derivative cell populations 2a and 2b (BMD2a and BMD2b). The metastasizing activity was compared between BMD1a cells and the parental D3H2LN cells. BMD1a cells produced brain metastasis in three out of five mice, whereas D3H2LN cells did in one out of 15 mice.

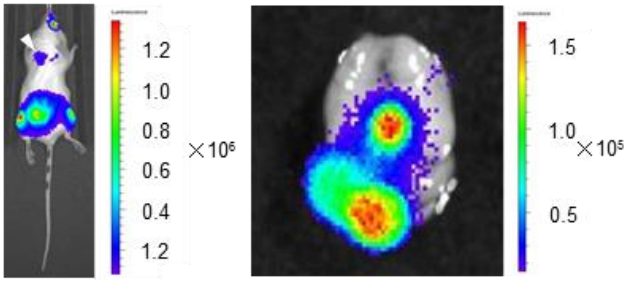

Fig 1b.
Bioluminescence image of a mouse with a BMD2a brain metastasis (left). Right image represents the bioluminescence image of a mouse brain with cancer cell metastasis.

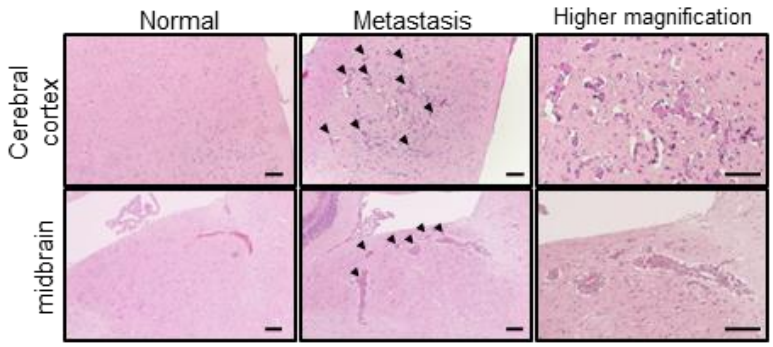

Fig 1c.
Representative image of hematoxylin and eosin (HE)-stained sections from a mouse brain cerebral cortex and midbrain. Left upper and lower panels show the mouse cerebral cortex and midbrain, respectively, without metastasis of cancer cells. Middle upper and lower panels show the mouse cerebral cortex and midbrain, respectively, with metastasis of cancer cells. Arrow head represent metastatic cancer cells. Right upper and lower panels show higher magnification. Bar represents 100 μm.

Blood-brain barrier *in vitro* model

To determine how EVs from breast cancer cells that metastasize to the brain affect BBB, the establishment of an *in vitro* BBB culture system that enables us to study the molecular and cellular effects of the EVs is essential. To this end, recent studies have employed monolayer cell culture systems[31]. However, BBB consists of three different types of cell, and these cells cooperate with each other to maintain the structure of BBB. Therefore, I employed a new *in vitro* BBB model system that consists of primary cultures of brain capillary endothelial cells, brain pericytes, and astrocytes (Fig. 1d).

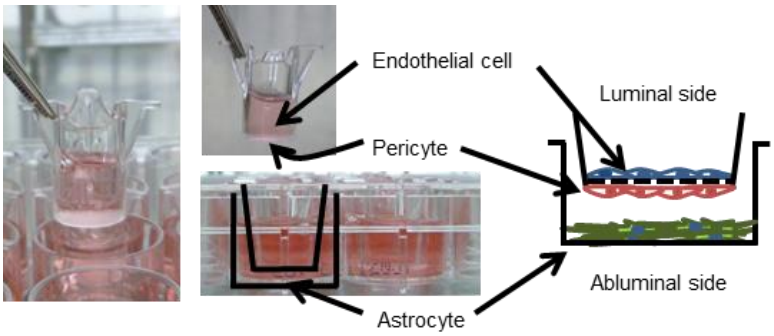

Fig 1d.
The schematic representation of the *in vitro* model of blood-brain barrier (BBB) constructed from primary cultures of monkey brain capillary endothelial cells, brain pericytes, and astrocytes.

As shown in Fig 1e, brain capillary endothelial cells, brain pericytes, and astrocytes were assessed using Hoechst 33342 staining. Furthermore, tight junction formations and adherens junction formations were confirmed with immunofluorescence analysis (Fig. 1f). These data supported the view that this *in vitro* BBB model simulated BBB *in vivo*. Moreover, transendothelial electrical resistance (TEER) was used to measure the formation of tight junctions by brain microvessel endothelial cells, which indicates the integrity of BBB. The TEER of this model is useful for the analysis of BBB *in vivo* (Fig. 1g)[32,33].

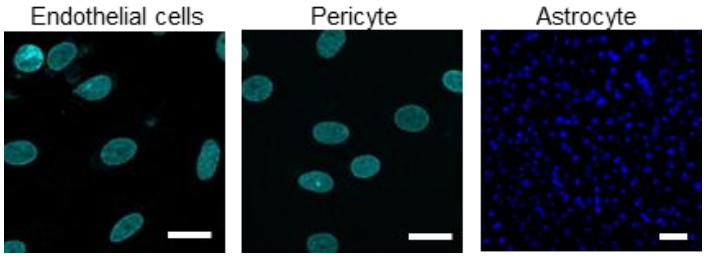

Fig 1e.

Representative pictures of endothelial cells, pericytes, and astrocytes are shown. Endothelial cells and pericytes were visualized using a confocal microscope. Astrocytes were visualized using a fluorescence microscope. Bar represents 20 μm. Bar in the panel of astrocytes represents 100 μm.

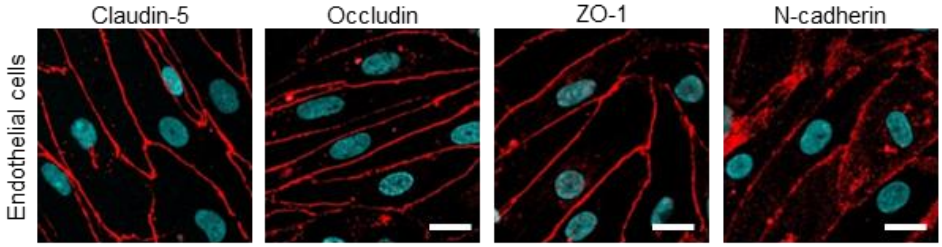

Fig 1f.

Immunofluorescence of tight junction proteins (Claudin-5, Occludin, and ZO-1) and N-cadherin (red). Bar represents 20 μm.

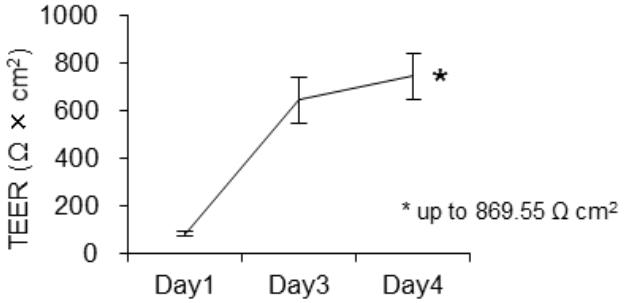

Fig 1g.

The transition of trans endothelial electric resistance (TEER) after thawing until the start of the experiment. After thawing the *in vitro* BBB model, the value of TEER increased to a maximum of 869.55 $\Omega \cdot cm^2$ (* mean maximum TEER.). Error bars represent S.D., *n* = 12. Data are representative of at least three independent experiments each.

Inhibition of EV secretion suppresses invasiveness through BBB

Because BBB consists of three different types of cells, knowing which cells incorporated EVs from cancer cells was essential for determining the precise mechanism of BBB destruction by EVs. The EVs from MDA-MB-231-luc-D3H1 (D3H1), D3H2LN, BMD2a, and BMD2b cell lines were typical in size (approximately 100 nm) and expressed conventional exosomal markers, such as CD63 and CD9 but not Cytochrome *C* (Fig. 2a, and 2b), which is a mitochondrial intermembrane-space protein known to be lacking in EVs[34].

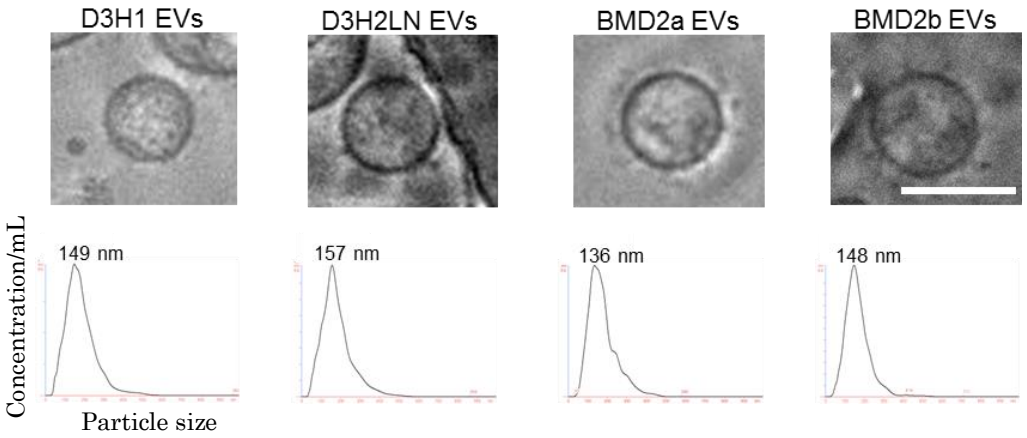

Fig 2a.

Phase-contrast electron microscopy was used to visualize resuspended EV pellets. Scale bar represent 100 nm. The sizes of EVs from MDA-MB-231-D3H1 (D3H1), MDA-MB-231-D3H2LN (D3H2LN), BMD2a, and BMD2b cells were measured by NanoSight. Numbers shown on graphs are the average sizes of all EV types.

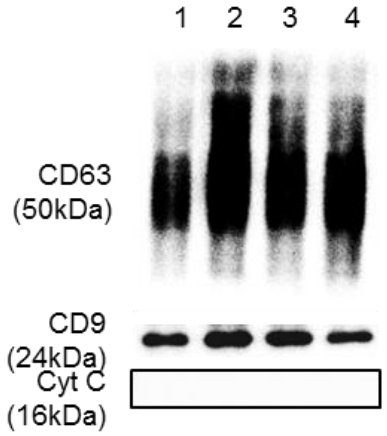

Fig 1b.
The conventional EV markers CD63 (500 ng/lane), CD9 (500 ng/lane), and Cytochrome C (3 μg/lane) were assessed by Western blot analysis. Lane 1: EVs from MDA-MB-231-D3H1; Lane 2: EVs from MDA-MB-231-D3H2LN; Lane 3: EVs from BMD2a; Lane 4: EVs from BMD2b.

The levels of EV secretion did not differ among the brain metastatic BMD2a, BMD2b, and D3H2LN cell lines (Fig. 2c). To this end, I added PKH67-labeled EVs isolated from BMD2a, BMD2b, and D3H2LN cells to the *in vitro* BBB model. As shown in Figs 2d and 2e, EVs from all cancer cells were incorporated into endothelial cells but not into pericytes or astrocytes. Interestingly, I observed higher fluorescent intensity in the endothelial cells with BMD cell-derived EVs, suggesting that BMD cell-derived EVs undergo tropism in brain endothelial cells (Fig. 2e).

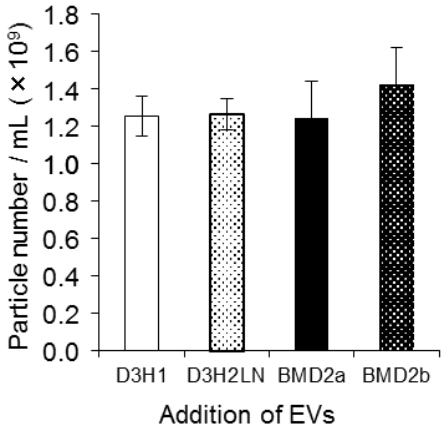

Fig 2c.

Number of EV particles isolated from each cell line as measured by NanoSight.

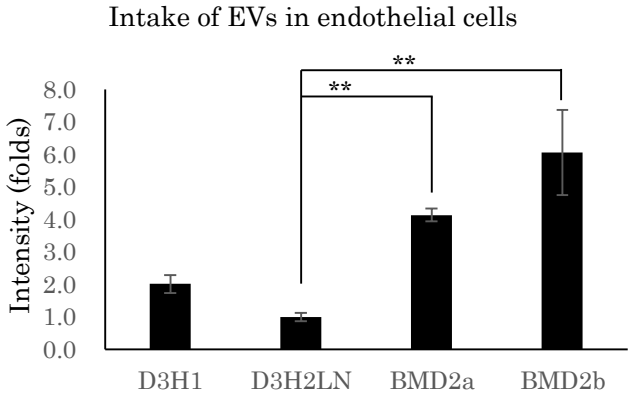

Fig 2d.

The intensity of PKH67-labeled EVs was measured by ImageJ. Error bars represent S.E., Student's T-test, $n = 3$. (** $P < 0.01$)

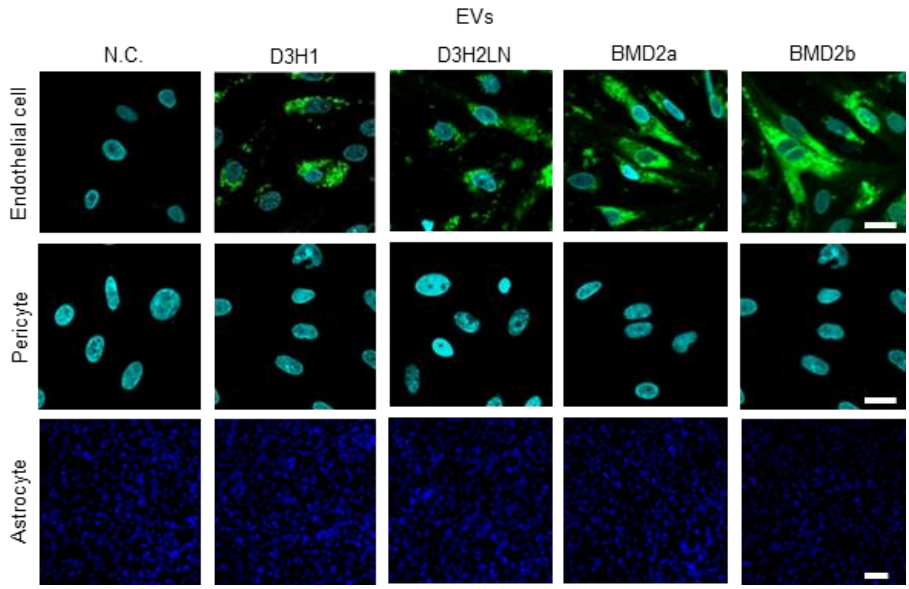

Fig 2e.

EVs isolated from cancer cells were labeled using PKH67 and added to the upper chamber. Representative pictures of endothelial cells, pericytes, and astrocytes are shown. Negative control (N.C.), EVs from MDA-MB-231-luc-D3H2LN (D3H2LN), EVs from BMD2a, and EVs from BMD2b are shown. Bar represents 20 μm. Bar in the panel of astrocytes represents 100 μm.

To determine whether the EVs from brain metastatic cancer cells functionally affected the destruction of BBB, I added D3H2LN cell-, BMD2a cell-, and BMD2b cell-derived EVs were added to the BBB model, and the TEER of each well was measured. As shown in Figs 2f and 2g, the TEER was significantly reduced in wells containing the BMD2a- or BMD2b cells-derived EVs compared with those containing the D3H2LN cells-derived EVs ($P < 0.05$).

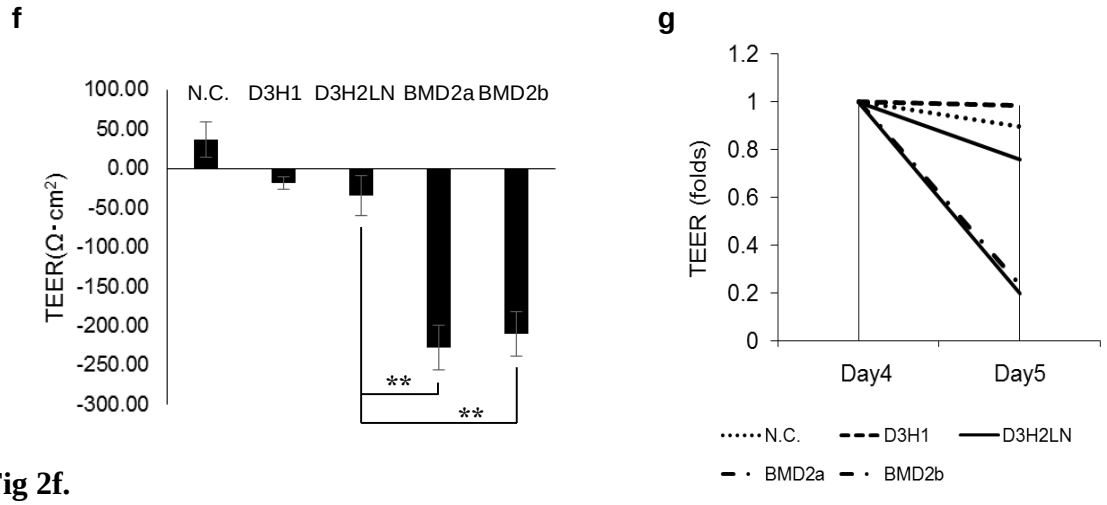

Fig 2f.

The value of the trans endothelial electric resistance (TEER) was monitored before (Day 4) and after (Day 5) the addition of EVs isolated from each cell line. EVs isolated from brain metastatic cancer cells were incubated in the *in vitro* BBB model for 24 hrs. Error bars represent S.E., Student's T-test, $n = 3$. (** $P < 0.01$, * $P < 0.05$)

Fig 2g.

The change in TEER after the addition of EVs. EVs from D3H1, D3H2LN, BMD2a, or BMD2b cells and negative control (N.C.) were added to the wells on day 4 after thawing of the *in vitro* BBB model. After 24 hrs, the TEER values were measured using an electrical resistance meter.

Furthermore, I tested the permeability of BBB using sodium fluorescein (NaF). Although the molecular weight of NaF is low (MW: 376.27), it cannot significantly permeate the intact BBB[35]. Therefore, NaF is used to assess the permeability of BBB by measuring its concentration with a fluorescence monochromator. NaF showed a high apparent permeability coefficient (Papp) in wells containing BMD2a cells- ($P < 0.01$) or BMD2b cells- ($P < 0.01$) derived EVs as compared with those containing EVs derived from the D3H2LN cell line or the D3H1 cell line (Fig. 2h).

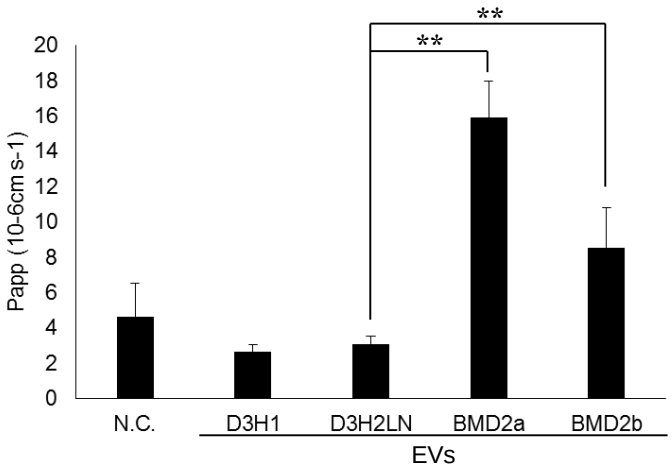

Fig 2h.

Assessment of BBB permeability determined by NaF (molecular weight = 376.27). EVs from MDA-MB-231-luc-D3H1 (D3H1), D3H2LN, BMD2a, or BMD2b cells and N.C. were added to the *in vitro* BBB model. After 24 hrs, NaF was added. NaF that had passed through BBB was measured by a fluorometer. Error bars represent S.E., Student's T-test, $n = 3$. (** $P < 0.01$)

Breast cancer cells are known to attach to microvessel endothelial cells to invade BBB (extravasation) during metastasis to the brain. Brain metastatic cancer cells are also considered to be highly invasive[22]. Matrigel invasion chamber assays were used to confirm the pathological implications of the metastatic potential of established cell lines. As shown in Figs 2i and 2j, BMD2a and BMD2b cells were more invasive than the D3H2LN cells or a low-metastatic D3H1 cells. However, the morphology of BMD2a and BMD2b cells did not differ from that of the D3H2LN cells (Fig. 2k).

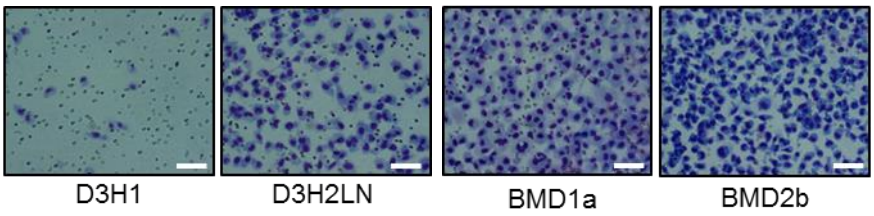

Fig 2i.

Representative images of invading cells, including D3H1, D3H2LN, BMD2a, or BMD2b. Bar represents 100 μm.

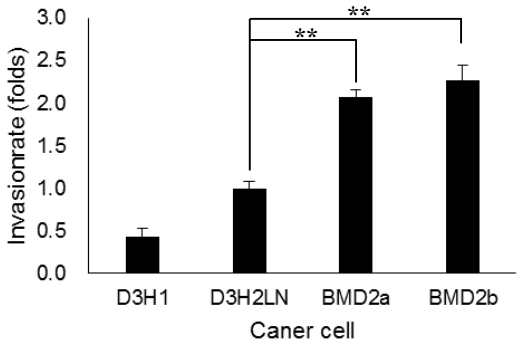

Fig 2j.

The invasion rate of BMD2a cells treated with siRNA against EV secretion-related proteins, such as nSMase2 and/or RAB27B and the transfection of control siRNA (N.C.). Inhibiting the production of EVs minimally inhibited the invasiveness of these cell lines, as assessed by a Matrigel^{TM} invasion assay. Error bars represent S.E., $n = 3$. (** $P < 0.01$)

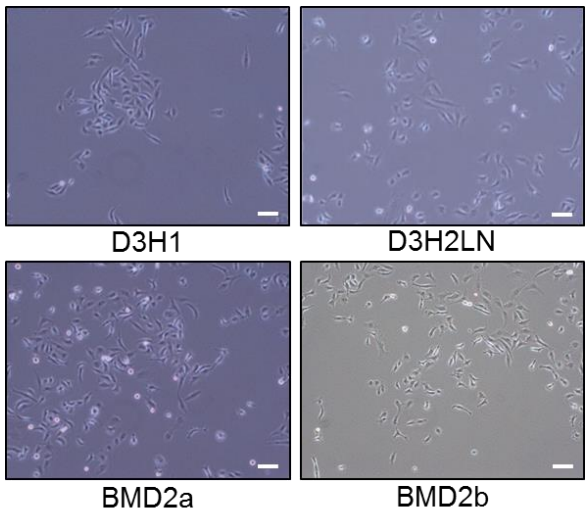

Fig 2k.

Representative cellular morphologies of D3H1, D3H2LN, BMD2a, and BMD2b cells. Bar represents 100 μm.

To confirm the extravasation of BMD2a and BMD2b cells into the brain parenchyma side of this model, D3H1, D3H2LN, BMD2a, and BMD2b cells were labeled with PKH26 to distinguish them *in vitro* and were added to the upper chamber of the *in vitro* BBB model. Cells that had infiltrated the abluminal side were counted after 2 days (Fig. 2l).

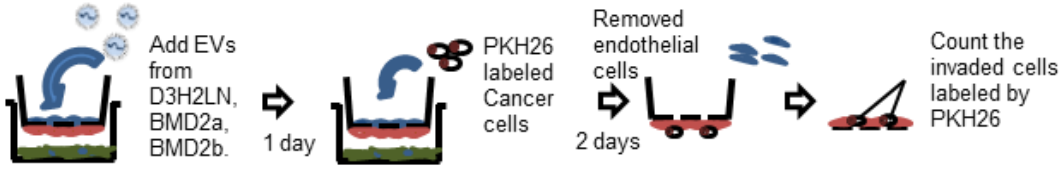

Fig 2l.
PKH67-labeled cancer cells (2×10^4 cells) were added to the *in vitro* BBB model. After a 48-hrs incubation, endothelial cells were removed, and the invading cells were counted using a fluorescence microscope.

As shown in Fig 2m, more BMD2a and BMD2b cells had extravasated compared with cells from the D3H2LN cells or the D3H1 cells, indicating that my established cell lines had a high potential for extravasation through BBB into the brain parenchymal side.

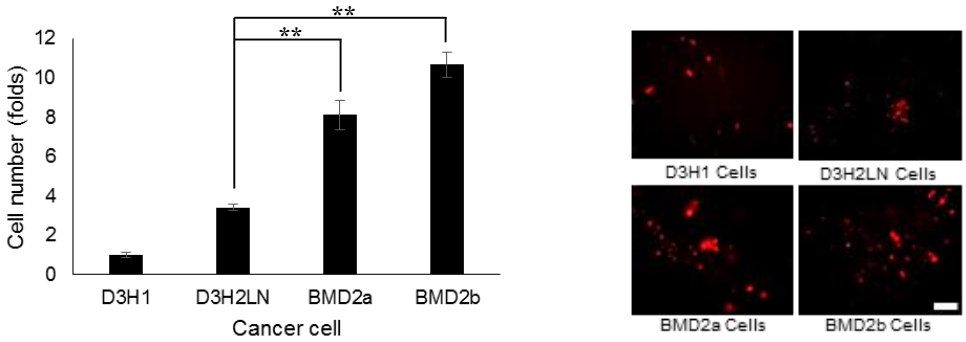

Fig 2m.
In vitro BBB transmigration activity of D3H1, D3H2LN, BMD2a, or BMD2b cells. The number of transmigrated cells relative to the D3H1 cell lines is plotted. Error bars represent S.E., Student's T-test, $n = 3$. (* $P < 0.05$, ** $P < 0.01$)

To clarify the contribution of EVs to the extravasation of brain metastatic cells, I assessed the extravasation of BMD2a cells in the *in vitro* BBB model after EV secretion in these cell lines was inhibited by siRNAs against EV secretion-related proteins, such as neutral sphingomyelinase 2 (nSMase2) and RAB27B (Figs. 2n, 2o and 2p)[8,36].

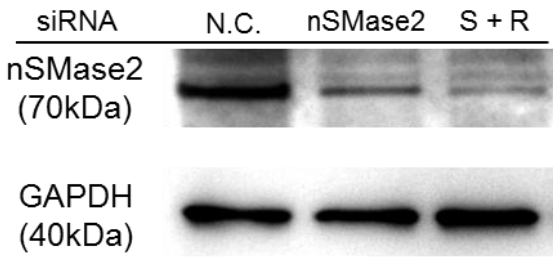

Fig 2n.
The expression of RAB27B mRNA in BMD2a cells after the transfection of control siRNA (N.C.), RAB27B siRNA, neutral sphingomyelinase 2 (nSMase2) siRNA, or nSMase2 and RAB27B siRNA (S+R). Error bars represent S.D., $n = 3$. (** $P < 0.01$)

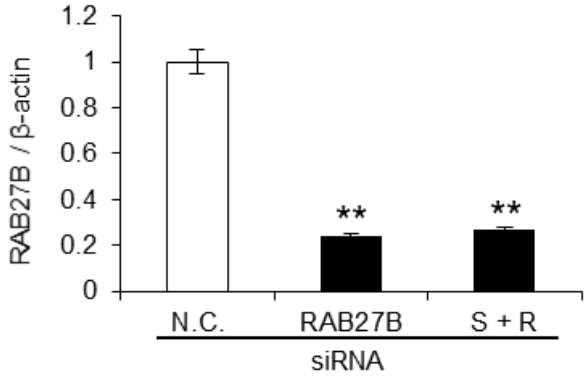

Fig 2o.
The expression of nSMase2 mRNA in BMD2a cells after the transfection of control siRNA (N.C.), nSMase2 siRNA, or nSMase2 siRNA and RAB27B siRNA (S+R). Error bars represent S.D., $n = 3$. (** $P < 0.01$)

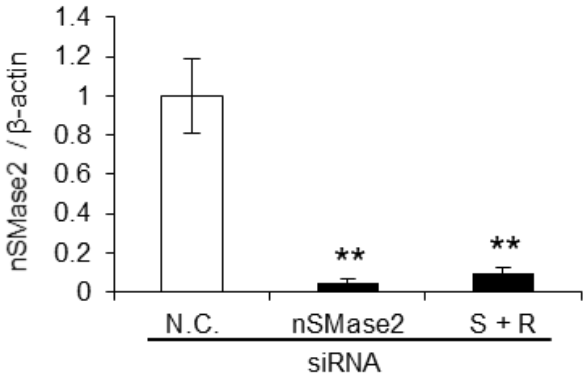

Fig 2p.
Western blot analysis of nSMase2, and GAPDH. Proteins from BMD2a cells treated with N.C. siRNA, nSMase2 siRNA, and nSMase2 + Rab27b siRNA.

PKH26-labeled cells treated with control siRNA could still pass through BBB to the abluminal side, but cells in which the production of EVs was inhibited (Fig. 2q) were not found on the abluminal side, even when those cells had the ability to pass through BBB (Fig. 2r).

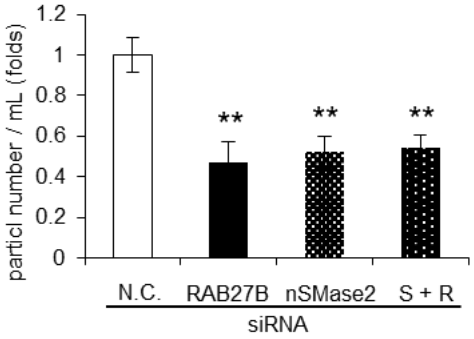

Fig 2q.
The number of EVs from siRNA-treated BMD2a cells. BMD2a cells were treated with siRNA against EV secretion-related proteins, such as nSMase2 and/or RAB27B and the transfection of control siRNA (N.C.). Error bars represent S.D., $n = 3$. (** $P < 0.01$)

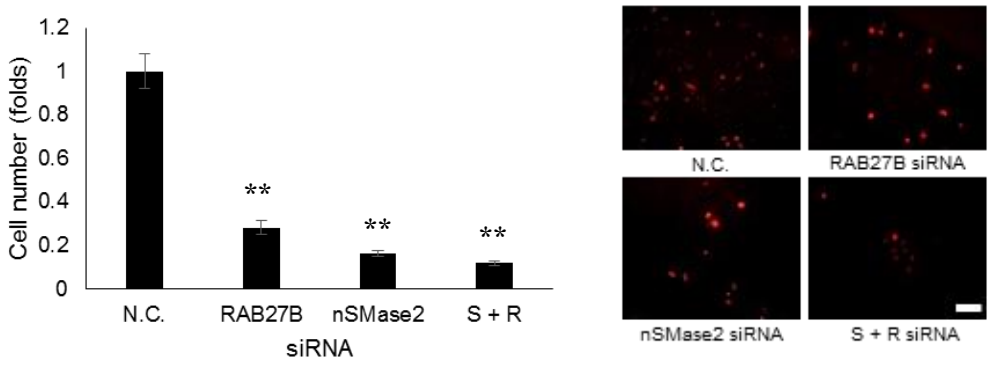

Fig 2r.

In vitro BBB transmigration activity of the BMD2a treated with control siRNA (N.C.), RAB27B, nSMase2, and both siRNAs (S + R). The number of transmigrated cells relative to the control cells is plotted. Error bars represent S.E., Student's T-test, $n = 3$. (** $P < 0.01$)

In addition, inhibiting the production of EVs slightly reduced the invasiveness of these cell lines, as assessed by a Matrigel invasion assay (Fig. 2s). This finding indicates that extravasation was not a result of the invasive potential of the cells. Furthermore, to investigate whether the addition of EVs is sufficient to allow the extravasation of cancer cells to the parenchymal side of the brain, I examined the extravasation of low-metastatic D3H1 cells after the addition of D3H2LN cells- and BMD2a cells- and BMD2b cells-derived EVs into the *in vitro* BBB model. The EVs isolated from BMD2a, BMD2b, or D3H2LN cells were added to each well and were incubated for 24 hrs before the addition of PKH26-labeled D3H1 cells. After 2 days, I counted the number of infiltrated cells. As shown in Fig 2t, D3H1 cells could not invade BBB without the addition of EVs. However,

infiltration of D3H1 cells to the abluminal side was significantly increased by the addition of BMD2a cells- or BMD2b cells-derived EVs. By contrast, the addition of D3H2LN cell-derived EVs did not efficiently promote the infiltration of low-metastatic D3H1 cells through BBB compared with BMD2a- and BMD2b cell-derived EVs. Taken together, these results suggest that the secretion of EVs by breast cancer cells affected the extravasation of metastatic cancer cells to the brain parenchyma side across BBB.

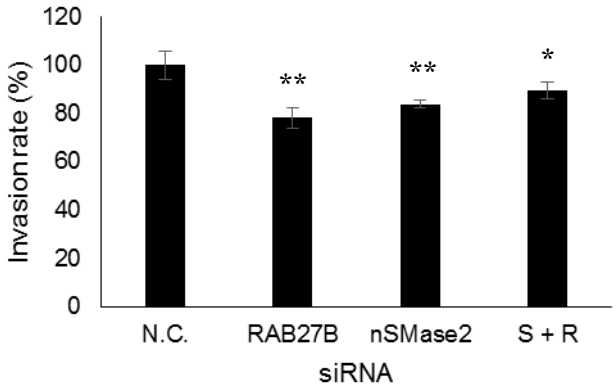

Fig 2s.

In vitro transmigration activity of the BMD2a cells. The number of transmigrated cells relative to the parental cell lines is plotted. Error bars represent S.E., $n = 3$. (* $P < 0.05$, ** $P < 0.01$)

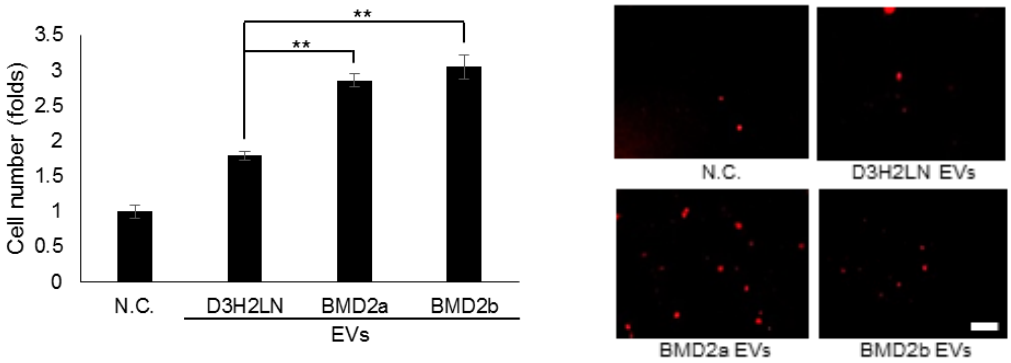

Fig 2t.

The number of transmigrated D3H1 cells relative to the control cells is plotted. Error bars represent S.E., Student's T-test, $n = 3$. (** $P < 0.01$) Data are representative of at least three independent experiments each.

Cancer cell-derived EVs promote brain metastasis *in vivo*

To evaluate the effect of cancer-derived EVs on the brains of mice, *in vivo* permeability assay was performed. Purified EVs derived from D3H2LN and BMD2a cells were labeled with a XenoLight DiR fluorescent dye before injection into the tail vein of mice. D3H2LN cell-derived EVs were used as a control. After 6 hrs, Tracer-653 probe, an *in vivo* tracer dye for monitoring BBB disruption, was injected into the mice. The upper panels of Fig 3a show the intake of EVs, and the lower panels show the permeability of brain blood vessels. As shown in the upper panels of Fig 3a, BMD2a cells-derived EVs were more incorporated in the brains of mice than D3H2LN cells-derived EVs. As shown in the lower panels of Fig 3a, BMD2a cell-derived EV-treated mice showed greater permeability of brain blood vessels as compared with D3H2LN cell-derived EV-treated mice *in vivo*.

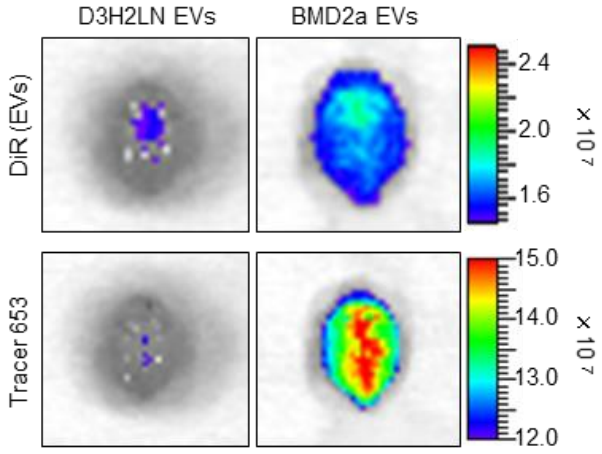

Fig 3a.
Fluorescence image of a mouse brain injected D3H2LN or BMD2a cell-derived EVs. The upper image represents the uptake DiR-labeled EVs of a mouse brain. The lower image represents the permeability of a mouse brain. D3H2LN cell-derived EVs were used as a control. This experiment was repeated twice.

Furthermore, to clarify the contribution of the EVs to brain metastasis in *in vivo*, D3H2LN cell- or BMD2a cell-derived EVs were injected in the tail vein of mice. After 24 hrs from the treatment with EVs, D3H2LN cells were injected in the left cardiac ventricle of mice; the mice were then observed after 18 days (Fig. 3b).

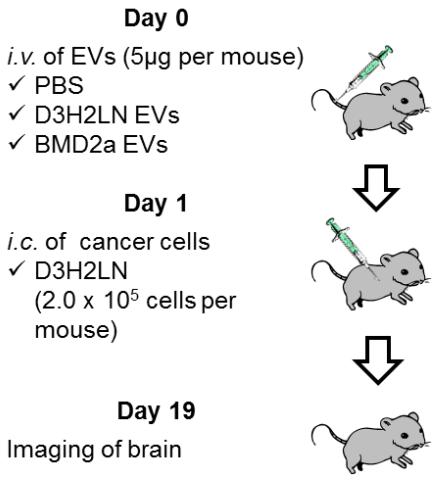

Fig 3b.
PBS (negative control), D3H2LN, and BMD2a-derived EVs (5 μg/mouse) were injected intravenously (*i.v.*) into C.B-17/Icr-scid/scid mice (Day 0). After 24 hrs, MDA-MB-231-D3H2LN breast cancer cell lines (2×10^5 cells) were injected intracardially (*i.c.*) into C.B-17/Icr-scid/scid mice (Day 1). After 18 days, the brain metastasis of cancer cells was monitored by *in vivo* imaging system (IVIS). $n = 9$ mice per group.

Brain metastasis rate after EVs treatment

Treatment	Brain metastasis, % (*n*)
N.C.	0% (0)
D3H2LN EVs	11.1% (1)
BMD2a EVs	55.6% (5)

Fig 3c.
The brain metastasis rate after EV treatment. $n = 9$ mice per group. D3H2LN-derived EVs were used as a control.

Importantly, mice treated with the BMD2a cell-derived EVs (brain metastases: 5 out of 9) had more brain metastases as compared to mice treated with D3H2LN cell-derived EVs (brain metastases: 1 out of 9) (Fig. 3c). Moreover, mice injected with BMD2a cell-derived EVs had a greater metastatic burden in the brain ($P < 0.05$, as measured by luciferase intensity, Fig. 3d) as compared to mice treated with D3H2LN cell-derived EVs (Fig. 3d). Negative control-injected mice were not observed to brain metastasis (Fig. 3c). In other words, mice treated with BMD2a cell-derived EVs had a higher rate of metastasis in the brain as compared to mice treated with the negative control or mice treated with EVs derived from the D3H2LN cells (Fig. 3e, lower panels, and Fig. 3c).

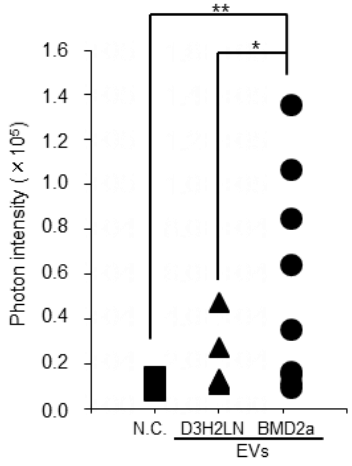

Fig 3d.
Distribution of photon intensity in the brain, quantified by ImageJ analysis. P-values were determined by Mann–Whitney one-tailed testing. Negative control (N.C.); $n = 9$, D3H2LN; $n = 9$, BMD2a; $n = 9$. (* $P < 0.05$, ** $P < 0.01$)

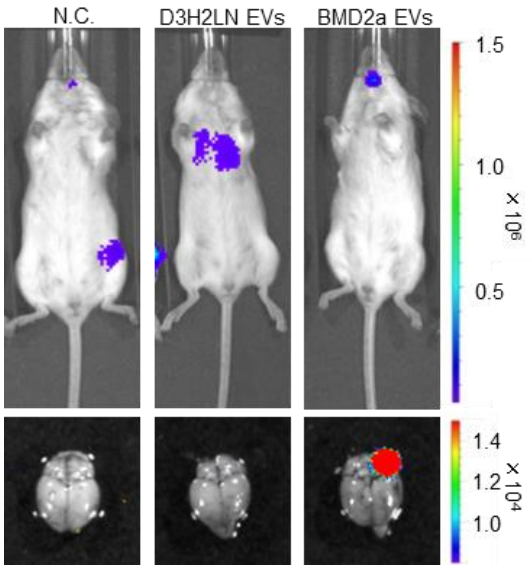

Fig 3e.
Bioluminescence image of D3H2LN and BMD2a cell-derived EVs and negative control (N.C.)- injected mice. The upper image represents the bioluminescence whole-body image of mice. The lower image represents the bioluminescence image of a mouse brain with cancer cell metastasis.

Brain metastasis was confirmed by hematoxylin and eosin (HE) staining and immunofluorescence staining against human vimentin (Fig. 3f). In mice treated with BMD2a cell-derived EVs, but not with D3H2LN cell-derived EVs, the presence of cancer cells in the brain was confirmed by HE-staining or immunofluorescence staining (Fig. 3f). These results show that BMD2a cell-derived EVs promoted brain metastasis by increasing the permeability of brain blood vessels which resulted in BBB breakdown.

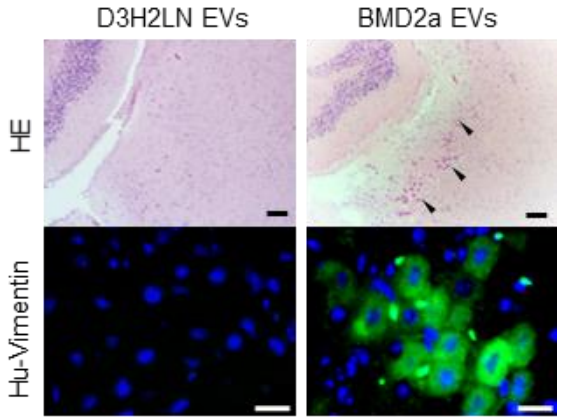

Fig 3f.

Representative image of hematoxylin and eosin (HE)-stained sections from a mouse brain cerebral cortex (upper panels). The arrowhead shows the cancer cells. Bar represents 100 μm. The lower panel shows a representative immunofluorescence image of anti-human vimentin (Hu-Vimentin). Bar represents 20 μm. Data are representative of at least three independent experiments each.

Disruption of intercellular junctions causes BBB breakdown

Tight junctions are known to regulate the low permeability of BBB and are formed by specific proteins in endothelial cells, such as Claudin-5, Occludin, and ZO-1. On the other hand, N-cadherin, a calcium-dependent cell-cell adhesion glycoprotein composed of five extracellular cadherin repeats that allow it to mediate strong cell-cell adhesion, is mostly expressed on the apical and basal membranes. Tight junction proteins and N-cadherin regulate cell polarity through their intimate association with the actin cytoskeletal network. From these aspects, I hypothesized that the breakdown of BBB might be caused by disregulation of these molecules. To prove this hypothesis, endothelial cells in the *in vitro* BBB model were co-immunofluorescently stained against Claudin-5, Occludin, ZO-1, and N-cadherin with actin filaments after the addition of EVs isolated from brain metastatic cancer cell lines or the D3H2LN cell line. Tight junction proteins were localized to the surface of the cell membrane in endothelial cells treated with PBS or EVs from D3H2LN cells; however, tight junction proteins and N-cadherin localized to the cytoplasm in cells that were treated with BMD2a cell- and BMD2b cell-derived EVs (Fig. 4a). Of note, I found that the expression of tight junction proteins, N-cadherin, and Actin was not affected by the addition of BMD2a cell- and BMD2b cell-derived EVs to brain blood vessel endothelial cells (Fig. 4b). These results strongly suggested that cancer-

derived EVs changed the localization of tight junction proteins, N-cadherin, and actin filaments, but did not affect the expression levels of these proteins.

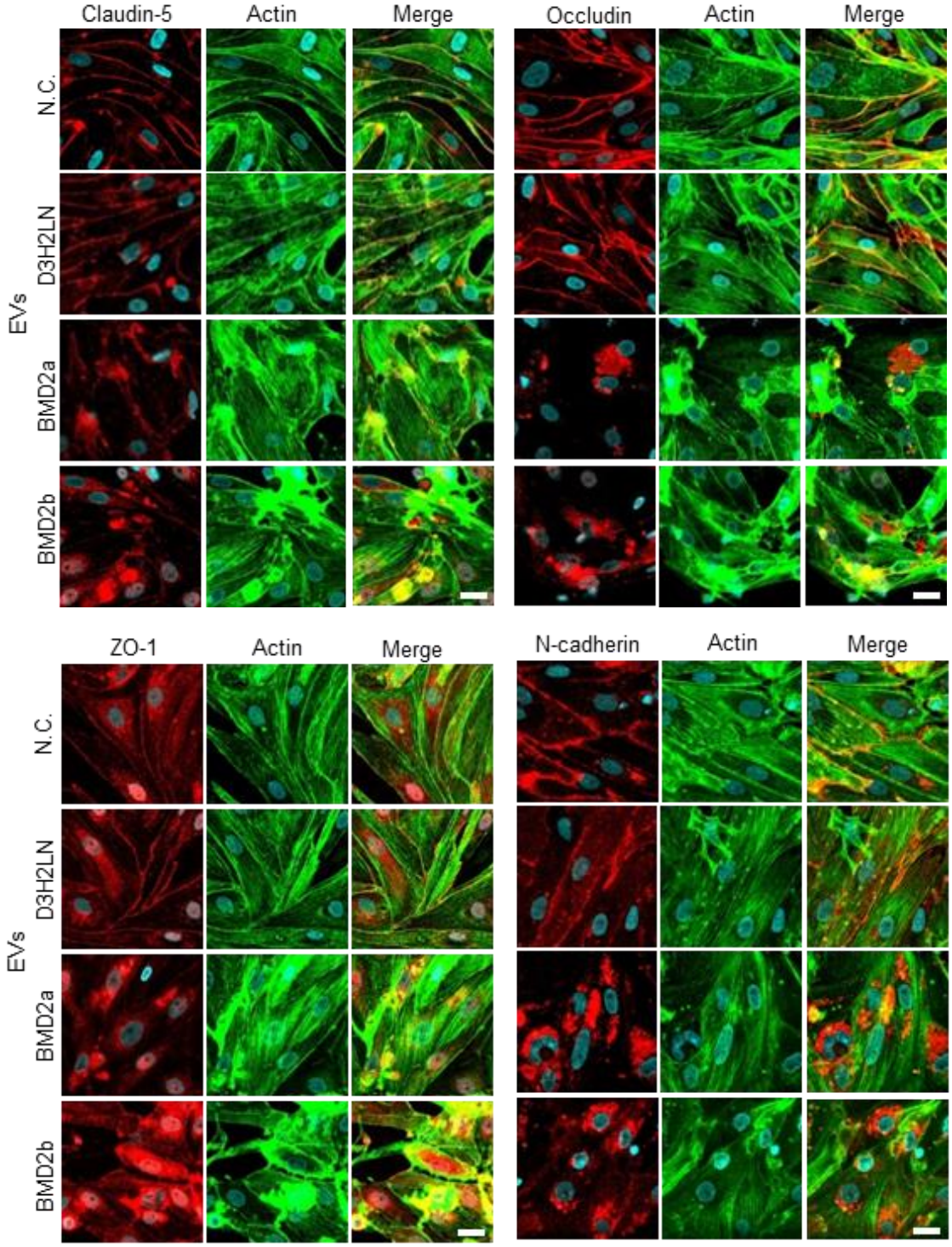

Fig 4a.

Co-immunofluorescence of tight junction proteins (Claudin-5, Occludin, ZO-1, and N-cadherin) (red) and actin filaments (green) after the addition of EVs from D3H2LN, BMD2a, or BMD2b cells. Bar represents 20 μm.

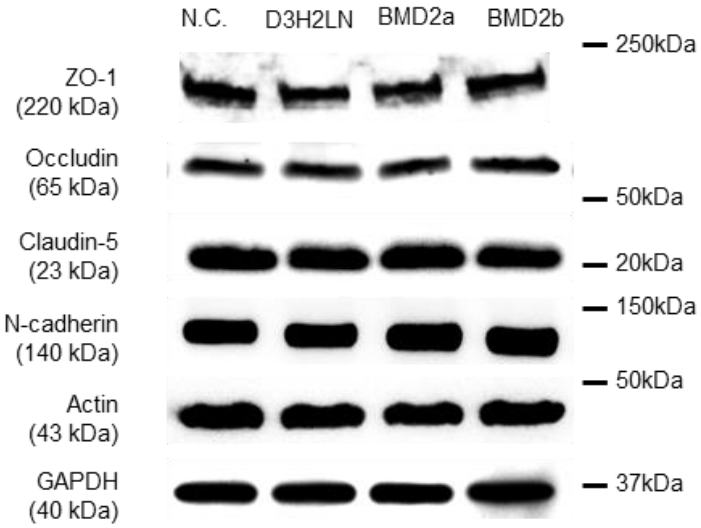

Fig 4b.

Western blot analysis of tight junction proteins, N-cadherin, Actin, and GAPDH. Proteins from endothelial cells treated with negative control (N.C.) or EVs. This experiment was repeated twice. Data are representative of at least three independent experiments each.

EV-contained miR-181c diminishes actin filament organization

To further investigate the molecular mechanisms by which EVs mediated the abnormal localization of tight junction proteins and adherence junction protein. I performed proteomic and miRNA microarray analyses of EVs isolated from BMD2a, BMD2b, and D3H2LN cells. In the proteomic analysis, I selected 15 proteins specifically expressed in BMD2a and BMD2b (The most significant 15 candidates are shown in Fig 5a). However, the association of these 15 protein candidates with BBB breakdown had not been reported.

Accession	Description
H2B1L	Histone H2B type 1-L
ENPP1	Ectonucleotide pyrophosphatase/phosphodiesterase family member 1
GNAS1	Guanine nucleotide-binding protein G(s) subunit alpha isoforms XLas
ITB4	Integrin beta-4
KPYM	Pyruvate kinase isozymes M1/M2
S38A2	Sodium-coupled neutral amino acid transporter 2
RAP1A	Ras-related protein Rap-1A
AMD	Peptidyl-glycine alpha-amidating monooxygenase
MARCS	Myristoylated alanine-rich C-kinase substrate
H2A1D	Histone H2A type 1-D
ACSL4	Long-chain-fatty-acid--CoA ligase 4
ACACA	Acetyl-CoA carboxylase 1
GBG2	Guanine nucleotide-binding protein G(I)/G(S)/G(O) subunit gamma-2
STOM	Erythrocyte band 7 integral membrane protein
GNA11	Guanine nucleotide-binding protein subunit alpha-11

Fig 5a.
Result of proteomic analysis. I selected specific proteins in BMD2a and BMD2b EVs compared with D3H1-derived and D3H2LN-derived EVs.

Furthermore, I performed miRNA microarray analysis in EVs. When the Cut-off value was decided over $\log_2$ 2.5, I found a total of 15 miRNAs that were up-regulated in BMD2a EVs and BMD2b EVs compared with D3H1-EVs and parental D3H2LN EVs.

		Log2[Sample/Control]					
	ProbeName	1-MM231-D3H1-Cell /2-MM231-D3H2LN-Cell	3-BMD2a-Cell /2-MM231-D3H2LN-Cell	4-BMD2b-Cell /2-MM231-D3H2LN-Cell	5-MM231-D3H1-Exo /6-MM231-D3H2LN-Exo	7-BMD2a-Exo /6-MM231-D3H2LN-Exo	8-BMD2b-Exo /6-MM231-D3H2LN-Exo
1	hsa-miR-4508	0	0	0	0	3.85	3.28
2	hsa-miR-3610	0	0	0	0	3.78	3.00
3	hsa-miR-663a	-2.19	1.70	1.29	0	3.34	2.64
4	hsa-miR-219-5p	-4.20	-0.43	-0.56	0	3.33	3.51
5	hsa-miR-340-5p	-0.50	-0.03	-2.84	0	3.18	2.93
6	hsa-miR-3200-3p	0	0	0	0	3.09	3.92
7	hsa-miR-4695-3p	0	0	0	0	3.03	3.06
8	hsa-miR-605	0	0	0	0	2.97	2.98
9	hsa-miR-6133	0	0	0	0	2.95	2.86
10	hsa-miR-764	0	0	0	0	2.85	3.06
11	hsa-miR-1273f	0	0	0	0	2.82	1.32
12	hsa-miR-670	0	0	0	0	2.80	3.10
13	hsa-miR-517a-3p	-2.38	0.40	0.29	0	2.61	2.91
14	hsa-miR-181c-5p	-2.25	-0.80	-0.87	0	2.54	2.41
15	hsa-miR-4750-5p	-0.49	0.15	0.13	0	2.52	2.81

Fig 5b.

Result of miRNA microarray analysis in D3H1-, D3H2LN-, BMD2a-, and BMD2b-derived EVs. I selected up-regulated miRNA in BMD2a and BMD2b-derived EVs compared with D3H1- and parental D3H2LN-derived EVs.

Finally, I found that miR-181c was significantly up-regulated in BMD2a cell- and BMD2b cell-derived EVs as compared with those derived from D3H2LN cells (Figs. 5c and 5d and 5e). No significant difference was observed in the cellular expression of miR-181c among D3H2LN, BMD2a, and BMD2b cells (Fig. 5f). Moreover, I assessed the expression of miR-181c in endothelial cells after the addition of EVs from breast cancer cells and found that its expression was significantly increased by the addition of EVs isolated from BMD2a and BMD2b cells (Fig. 5g).

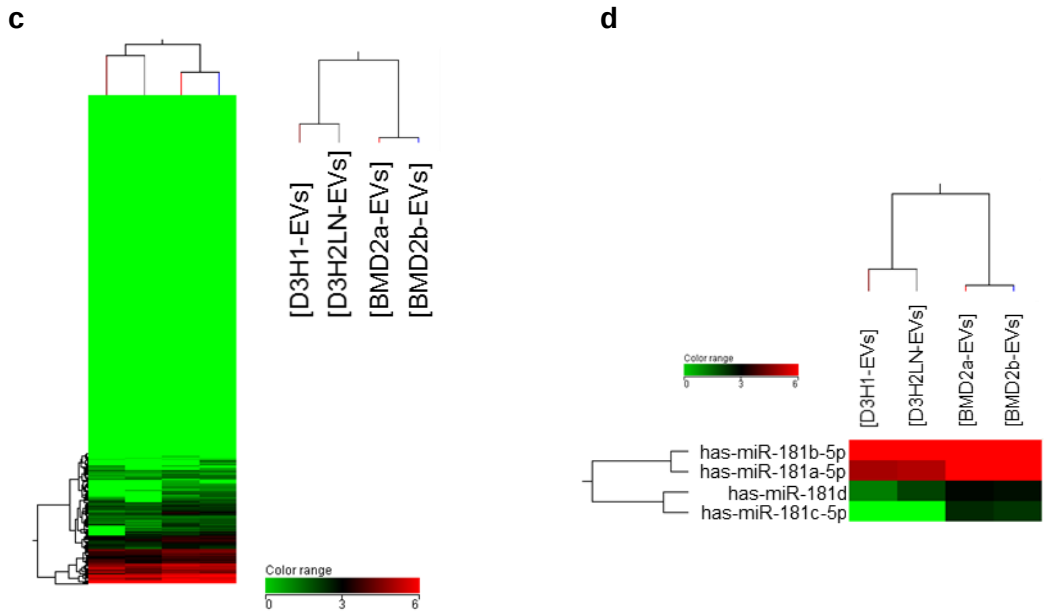

Fig 5c.
Heat map showing expression levels of the miRNAs in EVs isolated from MDA-MB-231-D3H1 (D3H1), MDA-MB-231-D3H2LN (D3H2LN), BMD2a, or BMD2b cells.

Fig 5d.
Heat map showing expression levels of the miR-181c in cancer-derived EVs.

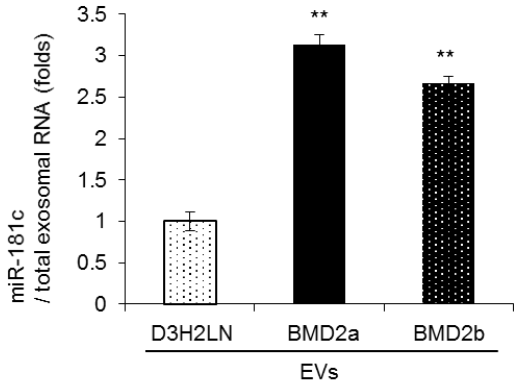

Fig 5e.

Amount of miR-181c in EVs isolated from D3H2LN, BMD2a, and BMD2b cells. Error bars represent S.D., Student's T-test, $n = 3$. ** $P < 0.01$ as compared with EVs from D3H2LN cells.

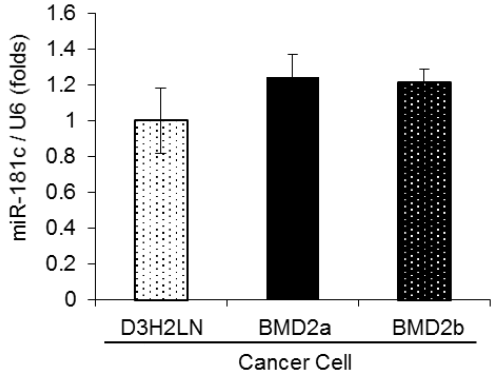

Fig 5f.

The expression levels of miR-181c in D3H2LN, BMD2a, and BMD2b cells were measured by qRT-PCR. Error bars represent S.D., $n = 3$.

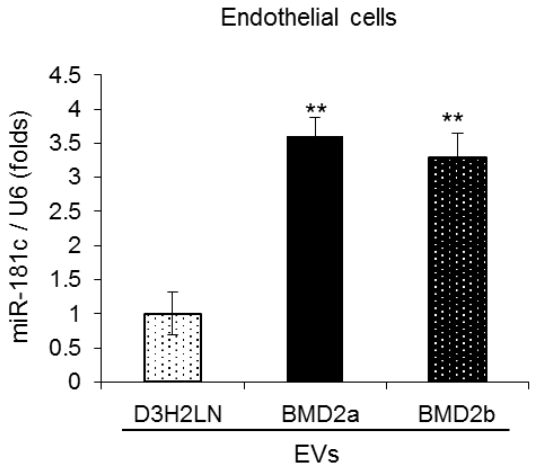

Fig 5g.

Endothelial cells were incubated with EVs isolated from D3H2LN, BMD2a, or BMD2b cells for 24 hrs. RNA was isolated from the endothelial cells 24 hrs after the addition of EVs, and the expression of miR-181c in the endothelial cells was analyzed by qRT-PCR. Each bar represents the mean S.D., Student's T-test, $n = 3$. ** $P < 0.01$ as compared with endothelial cells treated with EVs from D3H2LN cells.

To assess the direct effect of miR-181c on endothelial cells, synthetic miR-181c was transfected into endothelial cells from the *in vitro* BBB model. As shown in Fig 5h, tight junction proteins, N-cadherin, and actin localized to the cytoplasm in miR-181c-transfected cells, although localization of these molecules can be formed on membranes in negative control-treated cells.

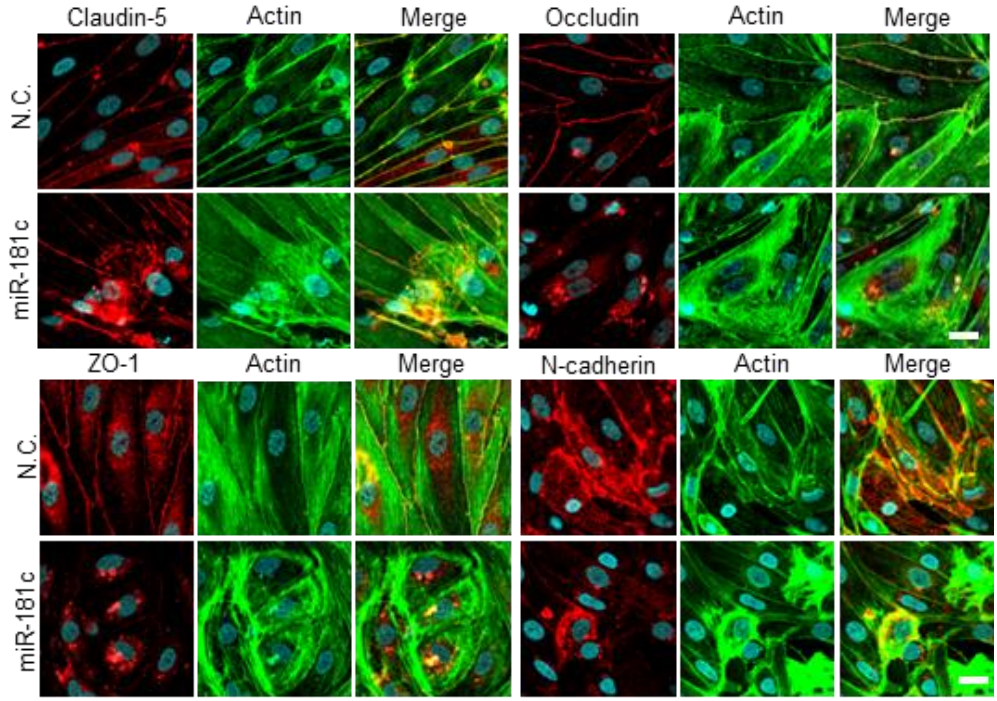

Fig 5h.

Coimmunostaining of Claudin-5, Occludin, ZO-1, N-cadherin (red), and actin filaments (green) in endothelial cells after the addition of EVs from D3H2LN, BMD2a, or BMD2b cells. Bar indicates 20 μm. These proteins localized to the cytoplasm in miR-181c-transfected cells.

Indeed, transfection of miR-181c significantly down-regulated the value of TEER in the *in vitro* BBB model (Fig. 5i). Furthermore, I found that the expression of tight junction proteins, N-cadherin, and Actin was not affected by the transfection of miR-181c into brain blood vessel endothelial cells (Fig. 5j).

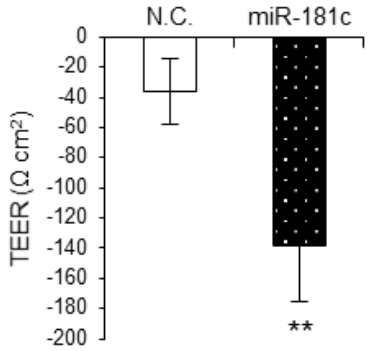

Fig 5i.

The trans endothelial electric resistance (TEER) value was monitored before (Day 4) and after (Day 5) the transfection of miR-181c or control siRNA. Transfected miR-181c or control siRNA was incubated in the *in vitro* BBB model for 24 hrs. Error bars represent S.D., Student's T-test, $n = 3$. (** $P < 0.01$)

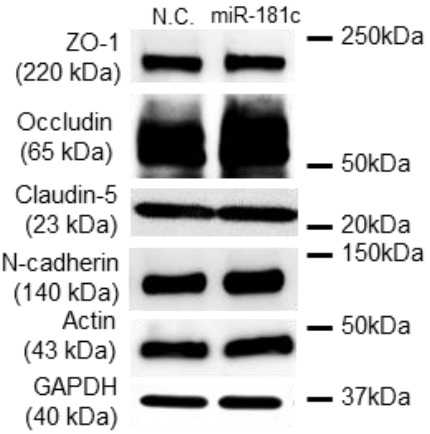

Fig 5j.

Western blot analysis of tight junction proteins, N-cadherin, Actin, and GAPDH. Proteins were from endothelial cells transfected with N.C. siRNA or miR-181c mimic. This experiment was repeated twice.

It is possible that miR-181c in EVs from brain metastasized cancer cells could be found in sera from breast cancer patients who have metastases in the brain due to the leakage of circulating EVs from brain metastatic cancer. To clarify this hypothesis, I analyzed the

expression abundance of miR-181c in sera from breast cancer patients (n = 56). As shown in Fig 5k, miR-181c in EVs collected from brain metastasis patients serum were significantly higher compared with non-brain metastasis patients (Brain metastasis; n = 10, Non-brain metastasis; n = 46, $P < 0.05$, *T-test*).

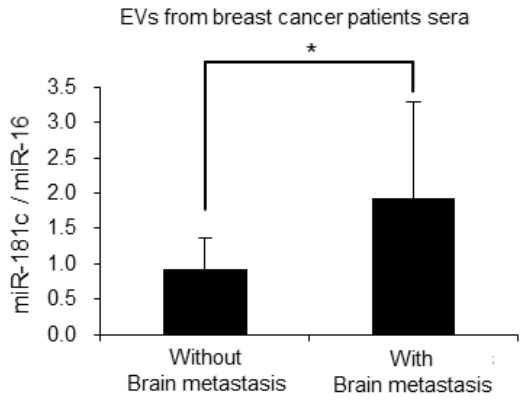

Fig 5k.
Amount of miR-181c in EVs isolated from patients' sera. Non-Brain metastasis: n = 46, Brain metastasis: n = 10. (* $P < 0.05$) Associations between the miR-181c expression levels of serum from breast cancer patients were assessed by T-test. Data are representative of at least three independent experiments each.

As shown in Fig 5l, the serum level of miR-181c was significantly higher in the sera from brain metastasis patients (stage IV; n = 10) as compared with the sera from non-brain metastasis patients (stage III; n = 13; $P < 0.05$, stage IV; n = 6; $P < 0.05$, *Mann-Whitney*

U test). Interestingly, in stage IV patients, the miR-181c level was higher in the sera from brain metastasis patients ($P < 0.05$). This result corroborated that secreting miR-181c is related to brain metastasis of breast cancer patients. Taken together, these results suggest that EVs from brain metastatic cancer cells induce the abnormal localization of tight junction proteins by transferring miR-181c into endothelial cells, which results in the destruction of the cell-cell contact.

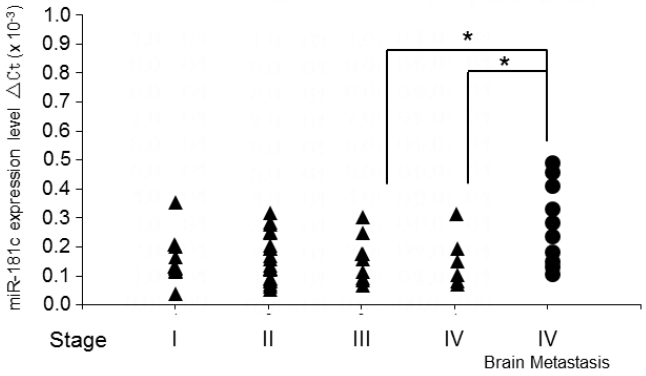

Fig 5l.
Expression level of miR-181c in total RNA from patients' sera. 1: stage 1 ($n = 10$); 2: stage 2 ($n = 22$); 3: stage 3 ($n = 9$); 4: stage 4 ($n = 6$); 5: brain metastasis patients ($n = 10$). (* $P < 0.05$, ** $P < 0.01$) Associations between the miR-181c expression levels of serum from breast cancer patients were assessed by Mann-Whitney U test.

PDPK1-regulated Actin localization is important to BBB

To understand in more detail the molecular mechanism of miR-181c in EV-mediated BBB destruction, I decided to identify the target gene of miR-181c in endothelial cells. I

performed global gene expression analysis in endothelial cells after the transfection of negative control or miR-181c (Fig. 6a, and 6b) and or after the addition of EVs from BMD2a, BMD2b, or D3H2LN cells (Fig. 6c, and 6d).

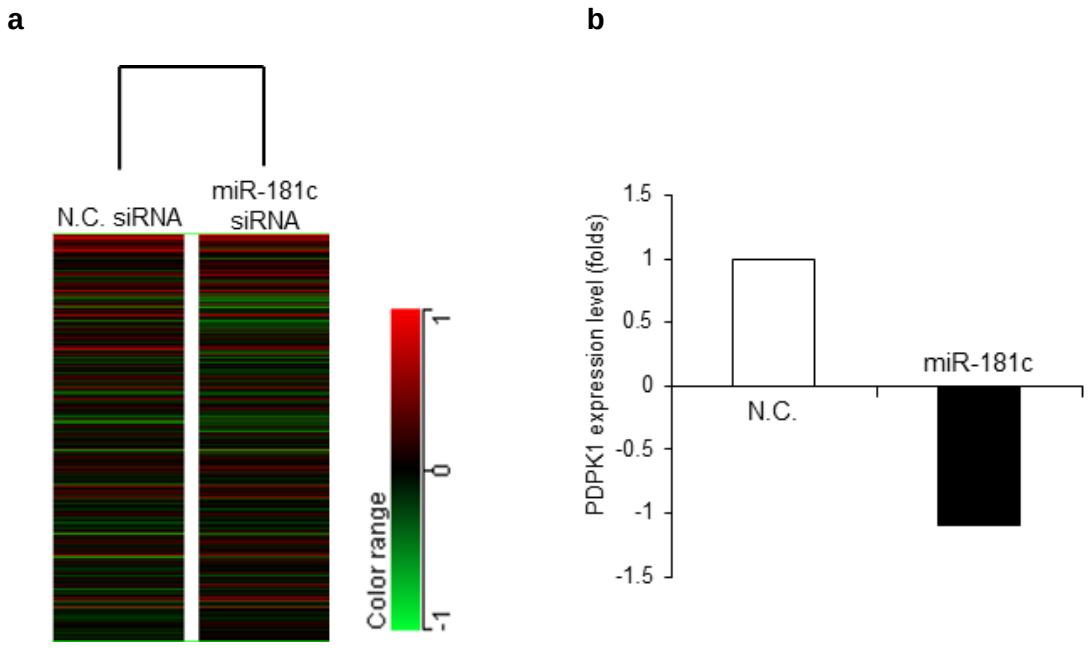

Fig 6a.
Heat map showing expression levels of the mRNAs in brain blood vessel endothelial cells transfected N.C. miRNA or miR-181c.

Fig 6b.
Microarray analysis showing expression levels of PDPK1 in brain endothelial cells after transfection of miR-181c. The data are represented as $\log_2$ value.

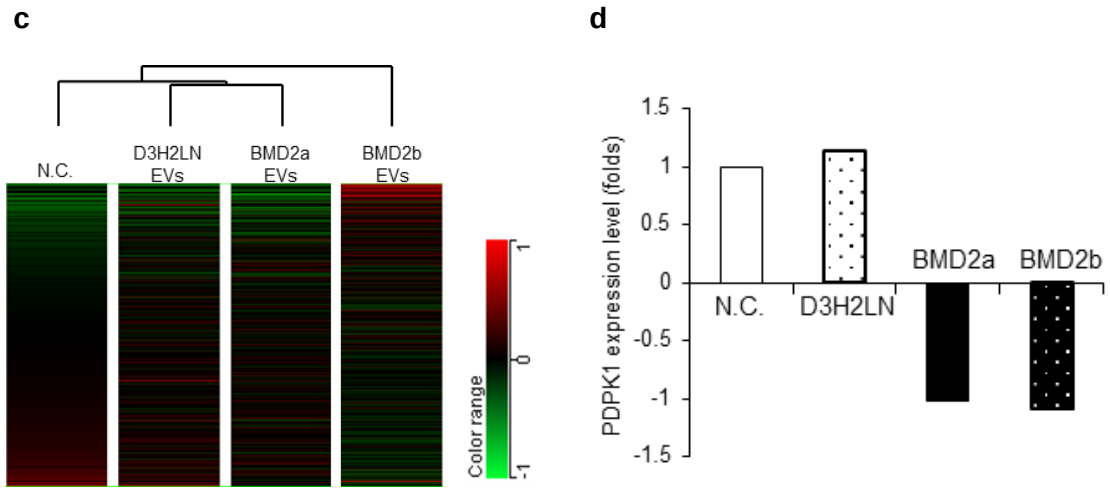

Fig 6c.
Heat map showing expression levels of the mRNAs in brain blood vessel endothelial cells treated EVs from MDA-MB-231-D3H1 (D3H1), MDA-MB-231-D3H2LN (D3H2LN), BMD2a, or BMD2b cells.

Fig 6d.
Microarray analysis showing expression levels of PDPK1 in brain endothelial cells after EV treatment.

I found that over-expression of miR-181c in brain endothelial cells exhibited down-regulation of 3-phosphoinositide-dependent protein kinase-1 (PDPK1) as compared with the control cells by mRNA and protein expression (Figs. 6e, and 6f). Furthermore, I also found that the expression of PDPK1 was down-regulated in BMD2a cell- or BMD2b cell-derived EV-treated endothelial cells as compared with that in D3H2LN cells by mRNA and protein expression (Figs. 6d, 6g, and 6h). These results suggest that miR-181c in EVs suppressed the expression of PDPK1 in brain endothelial cells.

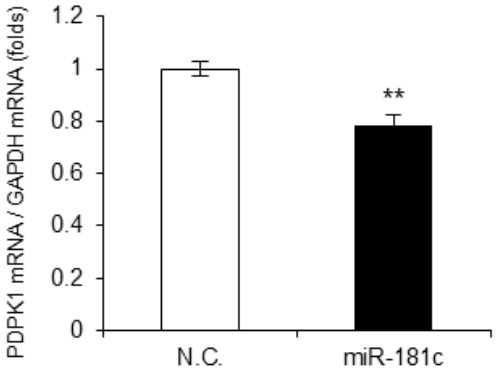

Fig 6e.

Expression level of PDPK1 mRNA in brain endothelial cells after the transfection of miR-181c. Error bars represent S.D., Student's T-test, $n = 3$. (** $P < 0.01$)

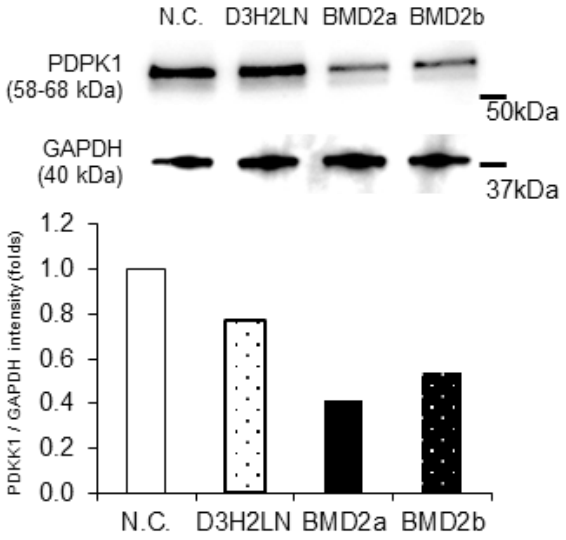

Fig 6f.

Western blot analysis of PDPK1 and GAPDH. Proteins were from brain endothelial cells treated with PDPK1 siRNA.

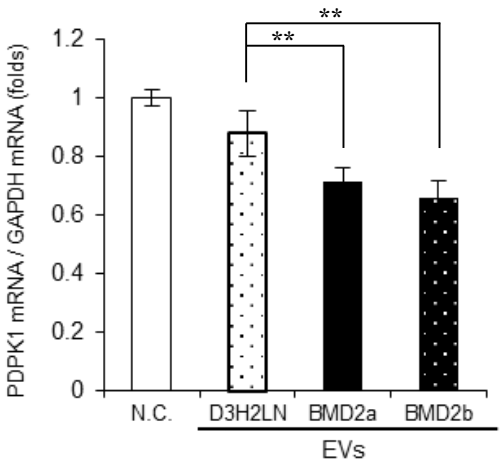

Fig 6g.

Expression level of PDPK1 mRNA in brain endothelial cells after the addition of EVs from D3H2LN, BMD2a, or BMD2b cells. Error bars represent S.D., Student's T-test, n = 3. (** $P < 0.01$)

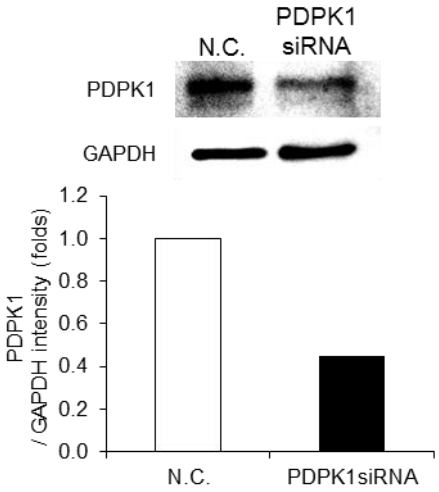

Fig 6h.

Western blot analysis of PDPK1 and GAPDH. Proteins were from endothelial cells treated with EVs from D3H2LN, BMD2a, or BMD2b cells. The lower panel shows the intensity of PDPK1 obtained from D3H2LN, BMD2a, or BMD2b cells. This experiment was repeated twice.

Next, I analyzed the effect of PDPK1 in the localization of tight junction-related proteins, N-cadherin, and actin filaments in brain endothelial cells after the treatment with PDPK1 siRNA. I showed that the expression of PDPK1 protein was down-regulated by the transfection of PDPK1 siRNA (Figs. 6i and 6j).

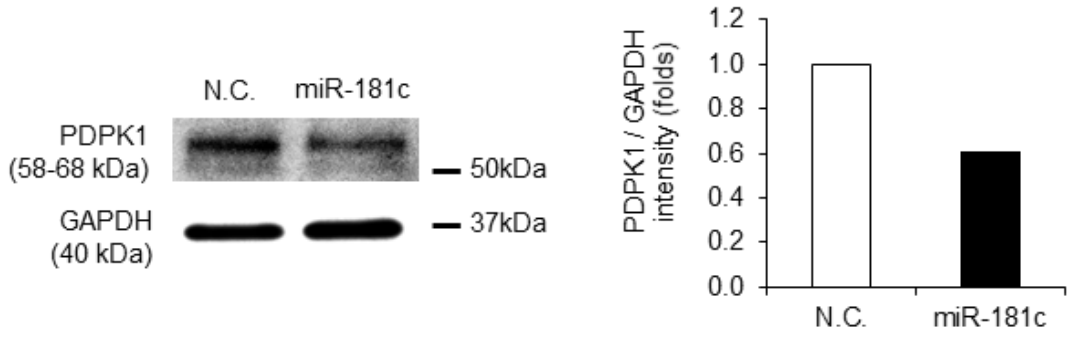

Fig 6i.
Western blot analysis of PDPK1 and GAPDH. Proteins were from brain endothelial cells treated with PDPK1 siRNA.

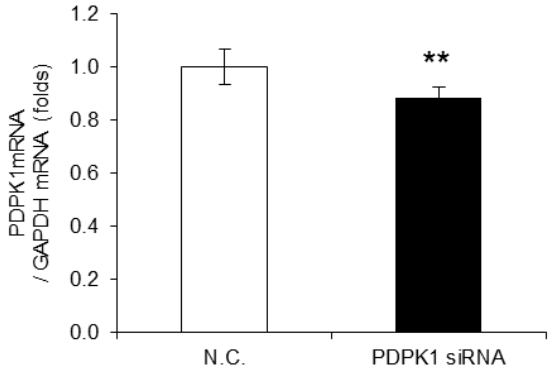

Fig 6j.
The expression levels of PDPK1 in brain endothelial cells after the transfection of PDPK1 siRNA were measured by qRT-PCR. Error bars represent S.D., $n = 3$.

As shown in Fig 7a, I observed the localization of tight junction proteins and N-cadherin at the cellular membrane in control siRNA-treated cells; however, these localizations were dysregulated in PDPK1 siRNA-treated cells. Localization of tight junction proteins, N-cadherin, and Actin was found in cytoplasm, whose results were the same as those of BMD2a cell- or BMD2b cell-derived EV-treated cells or miR-181c-transfected cells. Interestingly, Actin condensation was observed in the endothelial cells (Figs. 4a, 4b, 5f, and 7a).

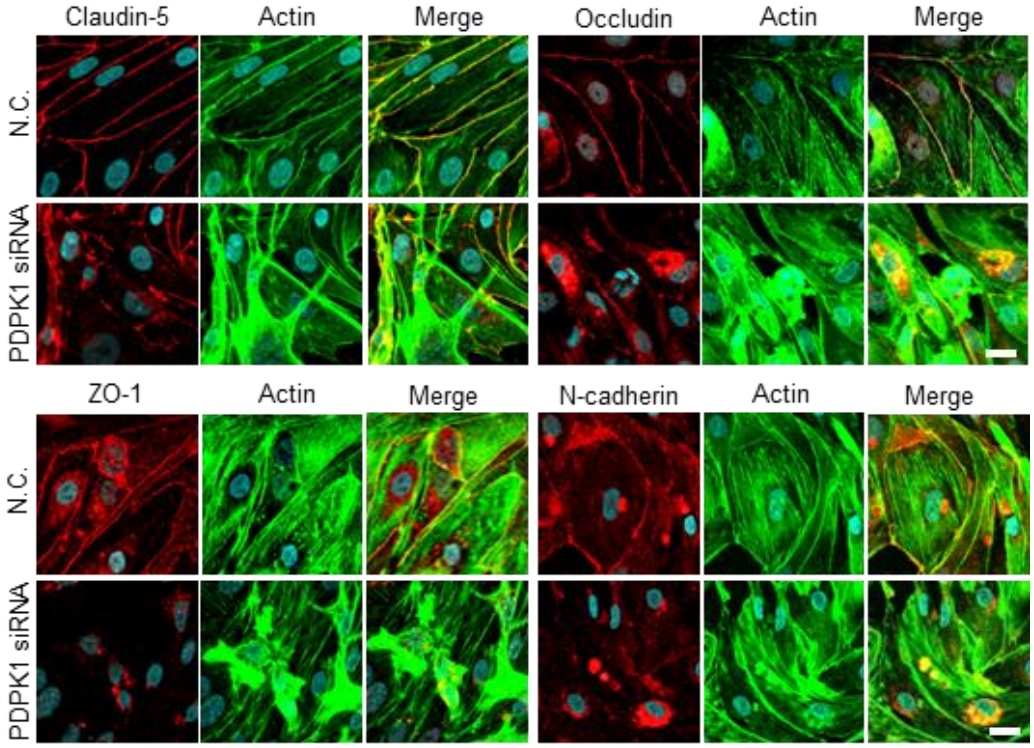

Fig 7a.
Co-immunofluorescence of tight junction proteins (Claudin-5, Occludin, and ZO-1), N-cadherin (red), and actin filament (green) after the addition of EVs from D3H2LN, BMD2a, or BMD2b cells. Bar represents 20 μm.

I confirmed that the expression of tight junction proteins, N-cadherin, and Actin proteins expression was not changed with or without PDPK1 siRNA treatment (Fig. 7b). The TEER of the *in vitro* BBB model was significantly down-regulated by PDPK1 siRNA treatment (Fig. 7c).

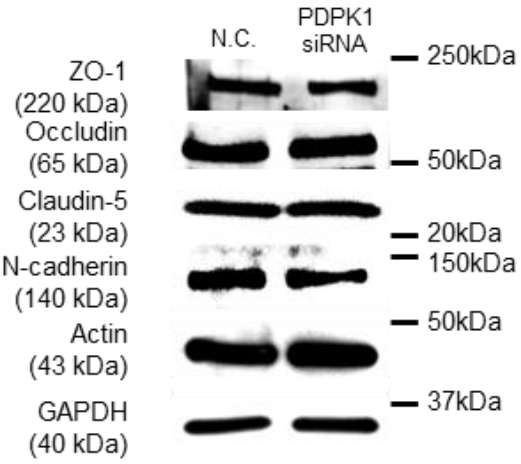

Fig 7b.

Western blot analysis of tight junction proteins, N-cadherin, Actin, and GAPDH. Proteins were from brain endothelial cells treated with PDPK1 siRNA. This experiment was repeated twice.

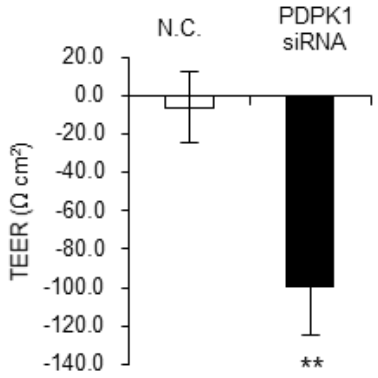

Fig 7c.

The TEER value was monitored before (Day 4) and after (Day 5) the transfection of PDPK1 siRNA or negative control. Error bars represent S.D., Student's T-test, $n = 3$. (* $P < 0.01$)

Furthermore, 3'UTR luciferase reporter assay was performed to analyze miR-181c and *PDPK1* mRNA. This result showed that 3'UTR of *PDPK1* was a direct target of miR-181c (Fig. 7d, and 7e).

PDPK1 mRNA 3'UTR sequence

Macaca 5'- TTGATGTACAGCCTTGAATGTGAATAATTATTGTAAACTATAT-3'
Human 5'- TTGATGTACAGCCTTGAATGTGAATAATTATTGTAAACTATAT-3'

miR-181c 3'-UGAGUGGCUGUCCAACUUACAA-5'

Fig 7d.
Schematics of the miR-181c binding site within the 3' UTR of the target mRNA.

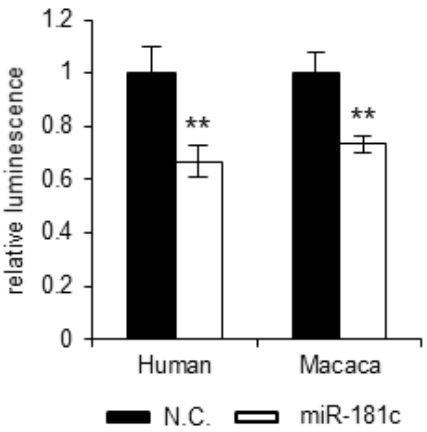

Fig 7e.
Luciferase activities measured by cotransfecting miR-181c and the PDPK1 luciferase reporters. Error bars represent S.D., Student's T-test, $n = 6$. (** $P < 0.01$)

Previous reports have shown that PDPK1 is an up-stream protein of cofilin phosphorylation[37,38]. Cofilin is a family of actin-binding proteins, which disassembles actin filaments, that is activated with dephosphorylation. Finally, western blot analysis of phospho-cofilin was performed. Phosphorylation of cofilin in BMD2a cell- or BMD2b cell-derived EVs-treated brain endothelial cells was down-regulated as compared with D3H2LN cell-derived EVs treatment (Fig. 7f). Furthermore, phosphorylation of cofilin in miR-181c or PDPK1 siRNA-treated brain endothelial cells was down-regulated as compared with negative control siRNA treatment (Fig. 7g). Taken together, these results suggest that miR-181c in EVs modulates the actin dynamics through the down-regulation of PDPK1 in brain endothelial cells (Fig. 8).

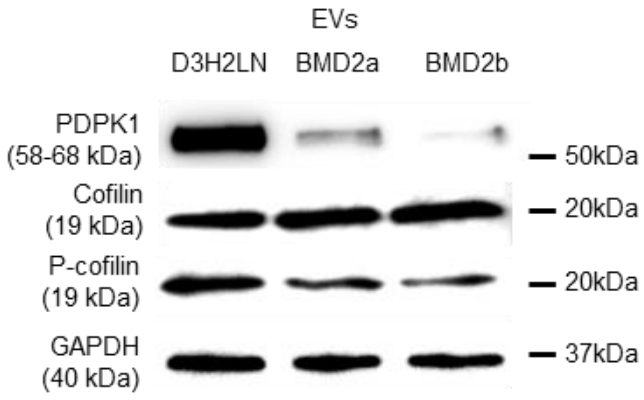

Fig 7f.
Western blot analysis of PDPK1, cofilin, phospho-cofilin (P-cofilin), and GAPDH. Proteins were from brain endothelial cells treated with EVs from D3H2LN, BMD2a, or BMD2b cells. This experiment was repeated twice.

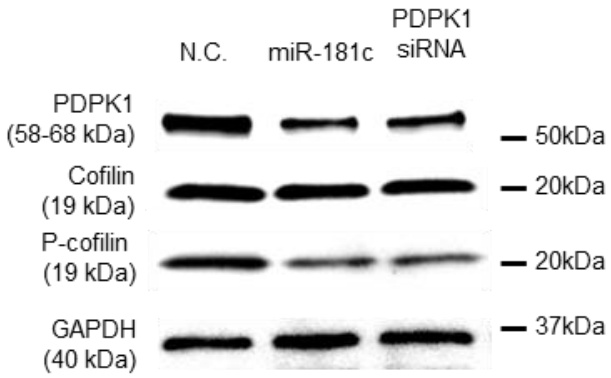

Fig 7g.

Western blot analysis of PDPK1, phospho-cofilin (P-cofilin), cofilin, and GAPDH. Proteins were from brain endothelial cells treated with miR-181c or PDPK1 siRNA. This experiment was repeated twice. Data are representative of at least three independent experiments each.

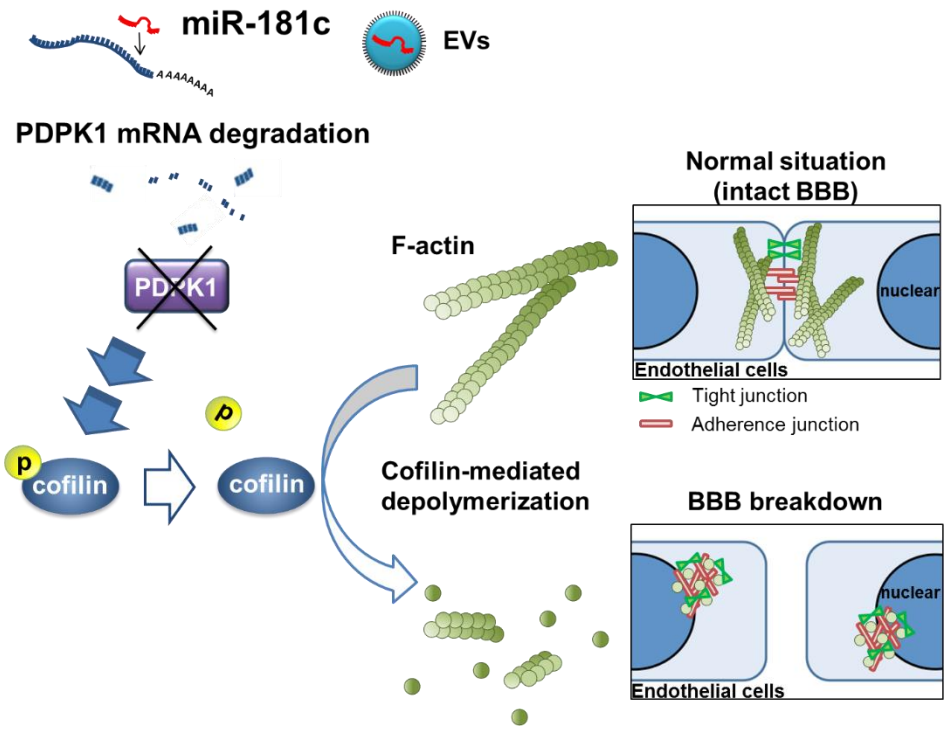

Fig 8.

Schematic model shows that miR-181c regulates de-phosphorylation of cofilin through PDPK1 expression. PDPK1 was suppressed by extracellular vesicles carrying miR-181c that was incorporated into brain endothelial cells. Activated cofilin is increased because PDPK1 was suppressed. Actin filaments are disassembled with activated cofilin. Tight junction proteins and cadherin were delocalized because actin filaments were destroyed.

6. Discussion

Circulating cancer cells have been shown to adhere to the brain blood vessel endothelium and, subsequently, to infiltrate the brain parenchyma[28]. During this event, cancer cells secrete humoral factors to induce the destruction of BBB and allow extravasation. Previous reports have shown that vascular endothelial growth factor (VEGF) expression of cancer cells was necessary but insufficient for the production of brain metastasis[29]. Bos *et al.* showed that the expression of ST6GALNAC5 in breast cancer cells enhances their adhesion to brain endothelial cells and their passage through the blood–brain barrier[30]. One of the key features of brain metastasis is the destruction of BBB[26]. In this manuscript, I have clearly shown that brain metastatic cancer cell-derived EVs trigger BBB destruction to promote the extravasation of cancer cells through BBB. BBB is composed of tight junction proteins, such as Claudin-5, Occludin, and ZO-1. The primary cytoskeletal protein, Actin, has known binding sites on all ZO proteins and on claudins and Occludin. Actin filaments serve both structural and dynamic roles in the cell[22]. Previous findings have shown that PDPK1 protein has a reduced F-actin to G-actin ratio[39] and is a critical regulator of actin polymerization[40]. Active cofilin is an actin-binding protein that severs filaments. Phosphorylation of cofilin through PDPK1 is thought to inactivate cofilin in a spatial manner in which local activation occurs at the cell membrane.

I have demonstrated that the actin dynamic in BBB was regulated with cancer-derived EVs in brain metastases. In this article, I have shown that PDPK1 was down-regulated by miR-181c in *in vitro* BBB model. Decreased PDPK1 in brain endothelial cells resulted in the breakdown of BBB by activated cofilin. Many reports have shown that miR-181c is related to malignancies such as hepatocellular carcinoma[41], basal cell carcinoma[42], and breast cancer[43]. Our results support the possibility that miR-181c plays an important role in malignancy.

Recently, Zhou *et al.* reported that breast cancer cell-derive EVs contributed to BBB breakdown[31]. Despite the significance of their findings, I should emphasize that our study is novel in the following points. First, our study suggests the possibility of organ tropism in brain metastasis of breast cancer cells. Zhou *et al.* revealed the possibility of the breakdown of the junctions between endothelial cells throughout the body. In contrast, our study focuses the brain-oriented metastasis of breast cancer, by establishing brain-oriented metastatic cell lines. Of note, I observed that EVs derived from these cell lines were more prone to accumulate in the brain than those from the parental cell line (Fig. 3a). Second, the mechanism described in the present study provides a novel miRNA-associated mechanism for EV-mediated BBB breakdown. Zhou *et al.*'s work suggests that miR-105 suppressed the ZO-1 expression in endothelial cells, and the resulting loss of

cell-cell adhesion lead to the promotion of metastasis. However, considering the capacity of EVs to harbor a variety of miRNAs, it seems difficult to conclude that a single EV-miRNA can explain the entire mechanism of BBB breakdown. In this regard, I revealed another novel mechanism in which miR-181c contributed to actin degradation through suppression of cofilin. Our findings, along with those by Zhou *et al.*, will help to understand the EV-mediated BBB breakdown.

Despite our observation that EVs accumulated preferentially in the brain, I have not yet identified molecules responsible for this organ tropism. Molecular analysis of EV membrane components will be of great importance to elucidate the organ tropism of metastatic cancer-derived EVs. In addition, the degree of contribution of EV-delivered miR-181c to BBB breakdown in the brain is not yet clear. Nevertheless, I have detected an increased level of circulating miR-181c in breast cancer patients with brain metastasis, suggesting an important role of secretory miR-181c in brain metastasis.

EVs as therapeutic targets might aid the prevention of BBB destruction in brain metastatic cancer and other diseases. The phenomenon of BBB destruction is not limited to brain metastases. BBB destruction is also known to be involved in diabetes, stroke, trauma, Alzheimer's disease, brain tumors, and malaria[44] that leads to disorders in brain function[16,45]. On the other hand, BBB destruction mechanism by cancer-derived

extracellular vesicles might be useful for drug delivery system for brain through BBB. This BBB breakdown mechanism includes the possibility of developing to drug-delivery system using EVs. Furthermore, EVs from cells contain multiple molecules, such as mRNAs, miRNAs, and proteins as well as membrane-associated molecules. These molecules might affect recipient cells in multiple ways and might contribute to target organ tropism of circulating EVs.

In conclusion, this study provides new insights into the mechanisms of brain metastatic cancer.

7. Future Perspective

The results of this project will apply to early diagnosis, cancer therapy, and drug delivery systems (DDS). For this project, I observed the brain tropism of EVs derived from an established cell line (BMD2a). However, the mechanisms of brain tropism of EVs are not clearly understood. Some reports have observed that EVs accumulate in the bone marrow, lungs, brain, lymph nodes, and tumor tissue46. However, these reports have not provided sufficient evidence supporting specific organ tropism. Nevertheless, “EVs are naturally occurring, nanosized vesicles that have attracted considerable attention as drug delivery vehicles in the past few years”. EVs have emerged as potential tools for DDSs to target organs or cells, and promising results have been achieved by using EV-based DDSs. In the future, I would like to apply a new DDS toward the identification of proteins that are responsible for the brain tropism.

8. Acknowledgment

I thank Dr. Hitoshi Nakagama, Dr. Takahiro Ochiya, Dr. Nobuyoshi Kosaka, Dr. Fumitka Takeshita, Dr. Yusuke Yoshioka and Dr. Takeshi Katuda for providing helpful discussion.

9. References

1 Valadi, H. *et al.* Exosome-mediated transfer of mRNAs and microRNAs is a novel mechanism of genetic exchange between cells. *Nat Cell Biol* **9**, 654-659 (2007).

2 Pan, B. T. & Johnstone, R. M. Fate of the transferrin receptor during maturation of sheep reticulocytes in vitro: selective externalization of the receptor. *Cell* **33**, 967-978 (1983).

3 Raposo, G. *et al.* B lymphocytes secrete antigen-presenting vesicles. *J Exp Med* **183**, 1161-1172 (1996).

4 Harding, C. V., Heuser, J. E. & Stahl, P. D. Exosomes: looking back three decades and into the future. *J Cell Biol* **200**, 367-371 (2013).

5 Yang, C. & Robbins, P. D. The roles of tumor-derived exosomes in cancer pathogenesis. *Clin Dev Immunol* **2011**, 842849 (2011).

6 Bobrie, A. *et al.* Rab27a supports exosome-dependent and -independent mechanisms that modify the tumor microenvironment and can promote tumor progression. *Cancer Res* **72**, 4920-4930 (2012).

7 Peinado, H. *et al.* Melanoma exosomes educate bone marrow progenitor cells toward a pro-metastatic phenotype through MET. *Nat Med* **18**,

883-891 (2012).

8 Kosaka, N. *et al.* Neutral sphingomyelinase 2 (nSMase2)-dependent exosomal transfer of angiogenic microRNAs regulate cancer cell metastasis. *J Biol Chem* **288**, 10849-10859 (2013).

9 Kosaka, N., Yoshioka, Y., Hagiwara, K., Tominaga, N. & Ochiya, T. Functional analysis of exosomal microRNA in cell-cell communication research. *Methods Mol Biol* **1024**, 1-10 (2013).

10 Rana, S., Malinowska, K. & Zöller, M. Exosomal tumor microRNA modulates premetastatic organ cells. *Neoplasia* **15**, 281-295 (2013).

11 Hannon, G. J. RNA interference. *Nature* **418**, 244-251 (2002).

12 Wilson, R. C. & Doudna, J. A. Molecular mechanisms of RNA interference. *Annu Rev Biophys* **42**, 217-239 (2013).

13 Fabbri, M. *et al.* MicroRNAs bind to Toll-like receptors to induce prometastatic inflammatory response. *Proc Natl Acad Sci U S A* **109**, E2110-2116 (2012).

14 Hood, J. L., San, R. S. & Wickline, S. A. Exosomes released by melanoma cells prepare sentinel lymph nodes for tumor metastasis. *Cancer Res* **71**, 3792-3801 (2011).

15 Gloor, S. M. *et al.* Molecular and cellular permeability control at the blood-brain barrier. *Brain Res Brain Res Rev* **36**, 258-264 (2001).

16 Abbott, N. J., Rönnbäck, L. & Hansson, E. Astrocyte-endothelial interactions at the blood-brain barrier. *Nat Rev Neurosci* **7**, 41-53 (2006).

17 Cardoso, F. L., Brites, D. & Brito, M. A. Looking at the blood-brain barrier: molecular anatomy and possible investigation approaches. *Brain Res Rev* **64**, 328-363 (2010).

18 Daneman, R., Zhou, L., Kebede, A. A. & Barres, B. A. Pericytes are required for blood-brain barrier integrity during embryogenesis. *Nature* **468**, 562-566 (2010).

19 Cunha-Vaz, J. G. The blood-retinal barriers system. Basic concepts and clinical evaluation. *Exp Eye Res* **78**, 715-721 (2004).

20 Wong, C. H., Mruk, D. D., Lui, W. Y. & Cheng, C. Y. Regulation of blood-testis barrier dynamics: an in vivo study. *J Cell Sci* **117**, 783-798 (2004).

21 Ohno, S., Ishida, M., Kataoka, A. & Murakami, S. Brain metastasis of breast cancer. *Breast Cancer* **11**, 27-29 (2004).

22 Arshad, F., Wang, L., Sy, C., Avraham, S. & Avraham, H. K. Blood-brain

barrier integrity and breast cancer metastasis to the brain. *Patholog Res Int* **2011**, 920509 (2010).

23 Bos, P. D., Nguyen, D. X. & Massagué, J. Modeling metastasis in the mouse. *Curr Opin Pharmacol* **10**, 571-577 (2010).

24 Winkler, E. A., Bell, R. D. & Zlokovic, B. V. Central nervous system pericytes in health and disease. *Nat Neurosci* **14**, 1398-1405 (2011).

25 Ballabh, P., Braun, A. & Nedergaard, M. The blood-brain barrier: an overview: structure, regulation, and clinical implications. *Neurobiol Dis* **16**, 1-13 (2004).

26 Lee, T. H., Avraham, H. K., Jiang, S. & Avraham, S. Vascular endothelial growth factor modulates the transendothelial migration of MDA-MB-231 breast cancer cells through regulation of brain microvascular endothelial cell permeability. *J Biol Chem* **278**, 5277-5284 (2003).

27 Nicolson, G. L. Organ specificity of tumor metastasis: role of preferential adhesion, invasion and growth of malignant cells at specific secondary sites. *Cancer Metastasis Rev* **7**, 143-188 (1988).

28 Orr, F. W., Wang, H. H., Lafrenie, R. M., Scherbarth, S. & Nance, D. M.

Interactions between cancer cells and the endothelium in metastasis. *J Pathol* **190**, 310-329 (2000).

29 Yano, S. *et al.* Expression of vascular endothelial growth factor is necessary but not sufficient for production and growth of brain metastasis. *Cancer Res* **60**, 4959-4967 (2000).

30 Bos, P. D. *et al.* Genes that mediate breast cancer metastasis to the brain. *Nature* **459**, 1005-1009 (2009).

31 Zhou, W. *et al.* Cancer-Secreted miR-105 Destroys Vascular Endothelial Barriers to Promote Metastasis. *Cancer Cell* **25**, 501-515 (2014).

32 Gaillard, P. J. *et al.* Establishment and functional characterization of an in vitro model of the blood-brain barrier, comprising a co-culture of brain capillary endothelial cells and astrocytes. *Eur J Pharm Sci* **12**, 215-222 (2001).

33 Wilhelm, I., Fazakas, C. & Krizbai, I. A. In vitro models of the blood-brain barrier. *Acta Neurobiol Exp (Wars)* **71**, 113-128 (2011).

34 Caby, M. P., Lankar, D., Vincendeau-Scherrer, C., Raposo, G. & Bonnerot, C. Exosomal-like vesicles are present in human blood

plasma. *Int Immunol* **17**, 879-887 (2005).

35 Nakagawa, S. *et al.* A new blood-brain barrier model using primary rat brain endothelial cells, pericytes and astrocytes. *Neurochem Int* **54**, 253-263 (2009).

36 Ostrowski, M. *et al.* Rab27a and Rab27b control different steps of the exosome secretion pathway. *Nat Cell Biol* **12**, 19-30; sup pp 11-13 (2010).

37 Lyle, A. N. & Griendling, K. K. Modulation of vascular smooth muscle signaling by reactive oxygen species. *Physiology (Bethesda)* **21**, 269-280 (2006).

38 Higuchi, M., Onishi, K., Kikuchi, C. & Gotoh, Y. Scaffolding function of PAK in the PDK1-Akt pathway. *Nat Cell Biol* **10**, 1356-1364 (2008).

39 Zaru, R., Mollahan, P. & Watts, C. 3-phosphoinositide-dependent kinase 1 deficiency perturbs Toll-like receptor signaling events and actin cytoskeleton dynamics in dendritic cells. *J Biol Chem* **283**, 929-939 (2008).

40 Lu, Z., Cox-Hipkin, M. A., Windsor, W. T. & Boyapati, A. 3-phosphoinositide-dependent protein kinase-1 regulates proliferation and survival of cancer cells with an activated mitogen-activated

protein kinase pathway. *Mol Cancer Res* **8**, 421-432 (2010).

41 Ji, J. *et al.* Identification of microRNA-181 by genome-wide screening as a critical player in EpCAM-positive hepatic cancer stem cells. *Hepatology* **50**, 472-480 (2009).

42 Sand, M. *et al.* Expression of microRNAs in basal cell carcinoma. *Br J Dermatol* **167**, 847-855 (2012).

43 Lowery, A. J. *et al.* MicroRNA signatures predict oestrogen receptor, progesterone receptor and HER2/neu receptor status in breast cancer. *Breast Cancer Res* **11**, R27 (2009).

44 Brown, H. *et al.* Evidence of blood-brain barrier dysfunction in human cerebral malaria. *Neuropathol Appl Neurobiol* **25**, 331-340 (1999).

45 Polimeni, M. & Prato, M. Host matrix metalloproteinases in cerebral malaria: new kids on the block against blood-brain barrier integrity? *Fluids Barriers CNS* **11**, 1 (2014).

46 Tominaga, N., Yoshioka, Y. & Ochiya, T. A novel platform for cancer therapy using extracellular vesicles. *Adv Drug Deliv Rev* (2015).